Orbital Level Understanding of Adsorbate-Surface Interactions in Metal Nanocatalysis

Siwen Wang

Dissertation submitted to the Faculty of the
Virginia Polytechnic Institute and State University
in partial fulfillment of the requirements for the degree of

Doctor of Philosophy
in
Chemical Engineering

Hongliang Xin, Chair
Luke E Achenie
Huiyuan Zhu
Eduard Faritovich Valeyev

May 19, 2020
Blacksburg, Virginia

Keywords: density functional theory, reactivity descriptor, chemisorption models, Bayesian learning

Orbital Level Understanding of Adsorbate-Surface Interactions in Metal Nanocatalysis

Siwen Wang

(ABSTRACT)

We develop a theoretical framework for a priori estimation of catalytic activity of metal nanoparticles using geometry-based reactivity descriptors of surface atoms and kinetic analysis of reaction pathways at various types of active sites. We show that orbitalwise coordination numbers CN^{α} ($\alpha = s$ or d) can be used to predict chemical reactivity of a metal site (e.g., adsorption energies of critical reaction intermediates) by being aware of the neighboring chemical environment, outperforming their regular (CN) and generalized ($\overline{CN}$) counterparts with little added computational cost. Here we include two examples to illustrate this method: CO oxidation on Au ($5d^{10}6s^{1}$) and O_2 reduction on Pt ($5d^{9}6s^{1}$). We also employ Bayesian learning and the Newns-Anderson model to advance the fundamental understanding of adsorbate-surface interactions on metal nanocatalysts, paving the path toward adsorbate-specific tuning of catalysis.

Orbital Level Understanding of Adsorbate-Surface Interactions in Metal Nanocatalysis

Siwen Wang

(GENERAL AUDIENCE ABSTRACT)

The interactions between reaction intermediates and catalysts should be neither too strong nor too weak for catalytic optimization. This Sabatiers principle arising from the scaling relations among the energetics of reacting species at geometrically similar sites, provides the conceptual basis for designing improved catalysts, but imposes volcano-type limitations on the attainable catalytic activity and selectivity. One of the greatest challenges faced by the catalysis community today is how to develop design strategies and ultimately predictive models of catalytic systems that could circumvent energy scaling relations. This work brings the quantum-chemical modeling and machine learning technique together and develops a novel stochastic modeling approach to rationally design the catalysts with desired properties and bridges our knowledge gap between the empirical kinetics and atomistic mechanisms of catalytic reactions.

Acknowledgments

I would like to thank my advisor Dr. Hongliang Xin for his continued guidance, inspiration and support throughout this project!

Many thanks to my committee members Luke E Achenie, Huiyuan Zhu and Eduard Faritovich Valeyev for their guidance of this project!

Special thanks to my families who encourage me to move on and my friends who keep me company!

Contents

List of Figures vii

List of Tables xi

1 Introduction 1

2 Coordination Numbers for Unraveling Intrinsic Size Effects in Gold-catalyzed CO Oxidation 4

2.1 Introduction 4

2.2 Computational details 6

2.3 Results and discussion 7

2.3.1 Comparison of different descriptors 7

2.3.2 Microkinetic Model 9

2.3.3 First-principles-based embedded atom method (EAM) 10

2.3.4 Size effect of Au nanoparticles toward CO oxidation 11

2.4 Conclusion 13

3 Overcoming Site Heterogeneity In Search of Metal Nanocatalysts 15

3.1 Introduction 15

3.2 Computational details 16

3.3 Results and discussion 18
3.3.1 Site heterogeneity of Pt nanoparticles toward oxygen reduction . . . 18
3.3.2 Orbitalwise coordination numbers as reactivity descriptors 20
3.3.3 Size effect of Pt nanoparticles toward oxygen reduction 23
3.3.4 Rapid screening of $A_3B@Pt_{ML}$ nanocatalysts 25
3.4 Conclusion 27

4 Bayesian Model of Chemisorption for Adsorbate-Specific Tuning of Electrocatalysis 28

4.1 Introduction 28
4.2 Computational Method 30
4.2.1 NewnsAndersonModel 30
4.2.2 Bayesian Inference 34
4.3 Results and discussion 34
4.3.1 *O adsorbed on the transition metals 37
4.3.2 *OH adsorbed on the transition metals 38
4.3.3 Density of states reconstruction and Sobol sensitivity 39
4.4 Conclusion 40

Bibliography 42

List of Figures

1.1 Catalytic reaction diagram. 2

1.2 Sabatier reactivity volcano. 3

2.1 (a) Linking the electronic structure of a surface metal site to its coordination number descriptors. (b) and (c) show the correlations of coordination numbers with adsorption energies of *CO and *O at an atop and a hollow site of Au nanoparticles, respectively. 8

2.2 Microkinetic analysis of CO oxidation on extended Au surfaces (a) (111), (b) (100), (c) (211), and (d) (532). Insets show the surface structure of DFT models. 9

2.3 (a) Cohesive energies of Au nanoparticles (not in the training set) from EAM potential optimization vs. that from GGA-PBE calculations. (b) Geometric strain of Au metal nanoparticles from EAM potentials, compared to the GGA-PBE functional and experimental measurements. 11

2.4 (a) Site population analysis of terrace and under-coordinated surface atoms of Wulff-constructed Au nanoparticles. (b) Experimental measured catalytic CO oxidation rates of supported Au nanocatalysts on irreducible metal oxides as a function of the size of metal nanoparticles. Model prediction based on the orbitalwise coordination number of EAM-optimized nanoparticles and volcano activity are shown to capture size effects of metal nanocatalysts. . . 12

3.1 ORR activity map of metal nanocatalysts. (a) Theoretical ORR limiting potential as a function of *OH and *OOH free formation energies. (b) Variations in the coordination environment of surface sites of a Pt_{201} nanoparticle quantified by the generalized coordination number $\overline{CN}$. Surface sites (1−6) are positioned on the activity map using DFT-calculated *OH and *OOH energies. 19

3.2 Orbitalwise coordination number as an activity descriptor. (a) *OH and *OOH free formation energies and (b) theoretical ORR limiting potential at surface sites of Pt nanoparticles described by the s-orbital based coordination number CN^s. A few model alloys with known ORR activity are located on the volcano plot based on the CN^s of the (111) terrace site of the 314-atoms Pt nanoalloys, illustrating the predictive power of the model. 20

3.3 The linear correlations of the s-orbital based coordination number CN^s with the *OH and *OOH free formation energies at various Pt sites including coinage metals in the core. 21

3.4 *OH and *OOH free formation energies using the d-orbital based CN^d as an activity descriptor. 22

3.5 Cohesive energies of Pt nanoparticles from the *ab-initio* EAM potential vs. that from GGA-PBE calculations in (a) training, (b) test. 23

3.6 Size effects of Pt nanoparticles toward oxygen reduction. (a) Model predicted vs. measured mass activity of Pt nanoparticles for oxygen reduction. The predicted activity is normalized using the highest mass activity. The *ab-initio* EAM potential was used for optimizing the geometric structures of a series of Wulff-constructed Pt nanoparticles. (b) Schematics of the nanoparticle model developed herein with the orbitalwise CN^{α} and the single-crystal model with the regular CN for predicting activity of metal nanocatalysts. 24

3.7 (a) Rapid screening of Pt monolayer core-shell nanoalloys A_3B@Pt_{ML} using the orbitalwise coordination number CN^s as a descriptor. 314-atoms nanoparticles with a 3:1 A:B ratio at the core were used (see the inset structural model). The activity is relative to Pt(111). The average activity and standard deviation of 5 random configurations in the core are reported. (b) Validation of model-predicted *OH free formation energies at identified alloys (5 sites for 5 core-randomalized alloys were used for Ru_3Ta@Pt_{ML}, Pd_3Cu@Pt_{ML}, and Pt_3Ni@Pt_{ML}). 25

4.1 The evolution of an adsorbate state (O^{2p}) upon adsorption (a)−(e) described by the Newns-Anderson model, using *O at the hollow site of Pt(111) as an example. 31

4.2 The binding energies of *O vs. *OH on {111}-terminated metal surfaces relative to H_2, H_2O. 35

4.3 (a) The co-variances and 1D histograms of joint posterior distributions of the model parameters (ΔE_{sp}, $\tilde{\epsilon}_a$, Δ_{sp}, α, and β) from MCMC simulations for *O adsorption at the fcc-hollow site of transition metals. 36

4.4 (a) Projected O^{2p} density of states from Bayesian learning(blue) and DFT calculations(orange). (b) DFT-calculated vs. model-predicted *O free formation energies on {111}-terminated transition metals 37

4.5 (a) Projected molecular orbital OH density of states from Bayesian learning(blue) and DFT calculations(orange). (b) DFT-calculated vs. model-predicted *OH free formation energies on {111}-terminated transition metals 38

4.6 (a) The reconstruction of density of states from moments using the maximum entropy algorithm. The projected d-states distribution of Pt(100) from DFT is shown together with the model distribution reconstructed from 15 lowest moments with and without a +2% perturbation to the band center ϵ_d. (b) Sobol sensitivity analysis of the Gaussian process regression model for *N free formation energies on Pt model alloys. 40

List of Tables

2.1 Embedded atom method potential parameters for Au trained with DFT GGA-PBE energies. 12

3.1 Embedded atom method potential parameters for Pt trained with DFT GGA-PBE energies. 25

Chapter 1

Introduction

Why do we care about catalysis? Well, simply because catalysis is everywhere. Catalysis is the cornerstone of modern chemical industry. The quality of our life depends heavily on the available natural resources including traditional fossil fuels, biomass in different forms, green electricity generated from wind turbine, wave power, photovoltaics, and the only really sustainable source of energy, the sunlight. To convert those natural resources into products we can use in our daily life and fuels which can be used by the vehicles, or simply speaking to break old chemical bonds and form new ones, we need catalysts. On the other hand, all those catalytic processes have side reactions leading to pollution in the air and water systems. In particular, the use of fossil fuels emits some hazardous gases and green house gases that contribute to the global warming and climate change. Again, to solve those problems, we need catalysts that are selective and efficient in breaking and forming chemical bonds.

So what is catalysis? The word "catalysis" was introduced into science by Swedish chemist Berzelius in 1800s. At that time, catalysis was something very hard to understand. Until 1900s, German chemist Wilhem Ostwald gave the modern definition of catalysis: "Catalysis is the acceleration of a slowly proceeding chemical reaction through the presence of a foreign substance". As shown in Fig. 1.1, for a simple reaction, A and B form C. First, A and B have to meet each other. The collision frequency is proportional to the concentration of [A] and [B]. It turns out that not all collisions can lead to reactions. To form a product, the reactants have to climb up the energy barrier. The probability of successful collisions depends on the

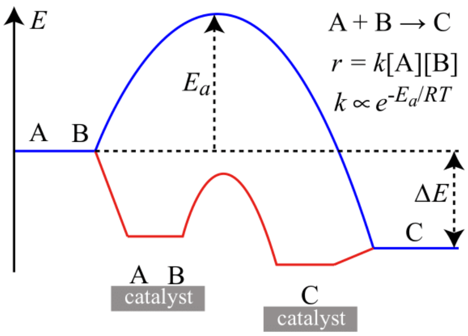

Figure 1.1: Catalytic reaction diagram.

system temperature and the energy barrier. What a catalyst does is to offer a facile path that has a lower barrier and so higher reaction probability. That is all it does. In general, there are three types of catalysts. Enzymes, made of large biological molecules, are vital to some very basic reactions in our body. Without those catalysts, we would not be able to survive. If the catalyst is in the same phase as the reactants and products, like the metal-organic complexes shown here, that is homogenous catalysis. For practical applications, you really want to be able to separate products from catalysts. So most of industrial chemical processes are catalyzed by solid materials.

For heterogeneous catalysis, there are different time and length scales and chemical reactions take place at the surface of the material. That is why nanoparticles are typically used, so you can have lots of surface area. No matter what reactions we are dealing with, macroscopic transformations can always be broken down into individual elementary steps that determine the overall efficiency of the process. For a catalyzed reaction, the catalyst needs to bring reactants down to the surface. The adsorbates can then diffuse to the active site, break required chemical bonds and form new ones. Eventually, the product desorbs and the active site is regenerated in this cycle. So this is the general approach I use and the scale I am focusing on during my PhD research.

The fundamental question is what defines a good catalyst? It has been recognized long time ago by Sabatier that the interaction between the catalyst and the critical surface intermediate should be just right; that is, neither too strong nor too weak, as shown in Fig. 1.2. The optimal catalyst is a compromise between the activity and availability of the active sites.

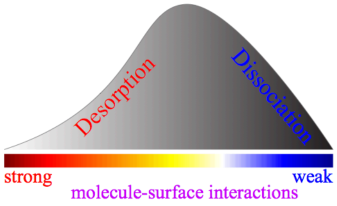

Figure 1.2: Sabatier reactivity volcano.

This simple picture is extremely useful for us to understand catalysis. But, there are two unfortunate consequences. One consequence is that because neighboring metal elements on the periodic table usually have very different affinity to molecules, it turns out that none of them is the optimal catalyst by itself. Of course, we can fine-tune its properties by mixing with other metal atoms, but without some practical guidance it is not easy. And people cannot just try all of them. Another consequence is that no matter how you tailor the bond energy between the molecule and surface, you are limited by an optimal catalytic activity. That is simply because when you speed up on step, you end up slowing down another step at the same time. You cannot tune both steps independently. That is really the curse here. To go beyond this limit, we have to control the dynamics of surface reactions by directing energy into one elementary step without slowing down others. Due to the lack of simple design principles, all of the industrial catalytic processes used today were developed based on tedious and costly experimental trial-and-error. And it is not surprising that the processes are far from optimized in terms of energy efficiency and environmental impact. To change the way the catalysts are being discovered, we really need to develop a fundamental understanding of energetics and dynamics of molecule-surface interactions.

Chapter 2

Coordination Numbers for Unraveling Intrinsic Size Effects in Gold-catalyzed CO Oxidation

2.1 Introduction

Bulk gold (Au) is chemically inert, while nanosized Au particles (<5 nm) are catalytically active[1]. Ever since its discovery by Haruta *et al.* in 1987, researchers have proposed many mechanisms to understand the observed CO oxidation activity trends, such as quantum size effects[2], under-coordinated atoms[3], charge transfer at interfaces[4], and strong metal/support interactions[5]. Certainly, complex metal/support interactions can not be overlooked; however, predicting catalytic activity of free-standing metal nanoparticles is crucial for rational design of catalysts with reduced cost and improved atomic efficiency.

The local chemical reactivity of metal nanoparticles are highly non-uniform across surface sites, which can be broadly divided into terrace, step, and kink types. Within the framework of the transition-state theory[6], the intrinsic kinetics of a surface reaction is governed by the thermodynamic stability of reaction intermediates and transition states at all accessible sites. Due to the complex interplay among size-dependent population of active sites, geometric strain of surface atoms, and quantum confinement of electronic states that overlap with valence orbitals of reacting species, one major challenge in catalysis is to know a priori catalytic outcomes of a nanoparticle. Direct computation of catalytic activity of a nanoparticle from quantum-chemical modeling is extremely time-consuming if not impossible. For this matter, understanding the effects of particle morphology on the interaction of surface atoms with adsorbates and thus reaction kinetics is of pivotal importance for identifying optimal active-site structures and engineering nanocatalysts with maximized fraction of such sites.

In this project, we propose an approach to a priori estimation of catalytic activity of metal nanoparticles using coordination numbers as reactivity descriptors of surface atoms and microkinetic analysis of reaction pathways at various types of active sites. We show that orbitalwise coordination numbers can be used to predict chemical reactivity of a metal site (e.g., adsorption energies of critical reaction intermediates) by being aware of the neighboring chemical environment, outperforming their regular (CN) and generalized ($\overline{CN}$) counterparts with little added computational cost[7]. To optimize geometric structures of metal nanoparticles, in particular for those systems that can not be directly simulated at the quantum-chemical level, we develop first-principles embedded-atom method (EAM) potentials trained with a limited number of DFT-GGA energies. Within this approach, we calculate the CO oxidation rate on a series of Wulff-constructed, free-standing Au nanoparticles, which shows a qualitative agreement with the activity trend of supported Au nanoparticles on a broad range of metal oxides. Utilization of various structure-reactivity models statistically illustrates the importance of under-coordinated atoms in understanding Au-catalyzed CO oxidation.

2.2 Computational details

All electronic structure calculations about Au systems were performed within the density functional theory (DFT) formalism implemented in GPAW (Grid-based Projector-Augmented Wave method) which applies PAW potentials to describe core electrons and the real-space grid to represent the electronic wavefunctions.[8, 9] Each nanoparticle was simulated in the centre of a simulation box while keeping at least 10 Å vacuum space of the particle surface away from the box boundary. All the extended surfaces were modeled by periodic four-layer slabs separated by 15 Å vacuum space along the norm of the surface, with 3 × 3 supercell for {100}, {111}, and {211} facets and 3 × 6 supercell for {532} facets. GGA-PBE functional was used to approximate exchange-correlation interaction and a grid spacing of 0.18 Å was chosen to describe the electronic wave functions. The Brillouin zones were sampled by the Γ-point for nanoparticles and by 4×4×1 Monkhorst-Pack k-points for extended surfaces.[10] The electronic occupation was smeared by the Fermi-Dirac distribution with a width of 0.2 eV to facilitate the SCF convergence, and all energies were extrapolated to T = 0 K. The structures of the bare metal nanoparticles and extended surface were fully relaxed with BFGS optimization method until the force on any atom was smaller than 0.05 eV/Å. For structure relaxation of the nanoparticulate systems with adsorbates, the adsorbates were allowed to relax while all the metal atoms were fixed at the optimized positions of bare systems. The relaxation energy of metal nanoparticles due to adsorption of CO and O is about constant, as verified for the Au201 nanoparticle (shown in our group's previous work[11]), thus not affecting the general descriptor-reactivity correlations.

The adsorption energies of CO and O were calculated as the difference between the electronic energy of the adsorbate-nanoparticle/slab complex and the sum of the electronic energies of the bare system and the adsorbates (CO or O):

$$\Delta E_{*CO} = E_{*CO} - (E_* + E_{CO}). \tag{2.1}$$

$$\Delta E_{*O} = E_{*O} - (E_* + E_{O_2}/2). \tag{2.2}$$

Where E_{*CO}, E_{*O}, E_*, E_{CO}, and E_{O_2} are electronic energies of the adsorbate-nanoparticle/slab complex, the bare nanoparticle/slab, gas phase CO and O_2 molecules. To avoid the difficulty in treating the triplet state of gas phase O_2, the electronic energy of O_2 was calculated from experimental H_2O formation energy and the electronic energies of gas phase H_2O, H_2.[12] For the convenience of following kinetic analysis, we have included the -0.2 eV for the gas phase CO because of the underestimation of CO formation energy using the PBE functional.[13]

2.3 Results and discussion

2.3.1 Comparison of different descriptors

The *d*-band chemisorption theory[14] linking the electronic structure of an active site to its local chemical reactivity provides a tremendous amount of understanding of what factors that characterize a good/bad catalyst. The electronic structure of pure metals, such as the *d*-band center, can be to a first order approximation related to the number of neighboring metal atoms, i.e., the regular coordination number (CN), providing an intuitive correlation between geometric and electronic structures of a surface site[15], see Fig. 2.1(a). A more rigorous count of neighbors using the generalized coordination number ($\overline{CN}$) proposed by Calle-Vallejo *et al.*, which weighs each neighboring atom by the ratio of its regular coordination number to that in the bulk, shows improved performance for capturing reactivity trends of Pt metal nanoparticles as oxygen reduction electrocatalysts[16].

A dual-descriptor model with the coordination number and curvature angle of surface metal atoms was proposed for capturing structural and reactivity properties of Au nanoclusters[17, 18]. However, for metal nanoparticles of d <5 nm (d: diameter), the strain of surface atoms ($\propto$ $1/d$) and quantum-size effects has to be considered. Recently, we have developed the orbitalwise coordination number defined in Eq. 2.3, that takes into account the orbital symmetry of any atom identity and broken-bond strain of neighboring atoms as shown in Fig. 2.1(a).

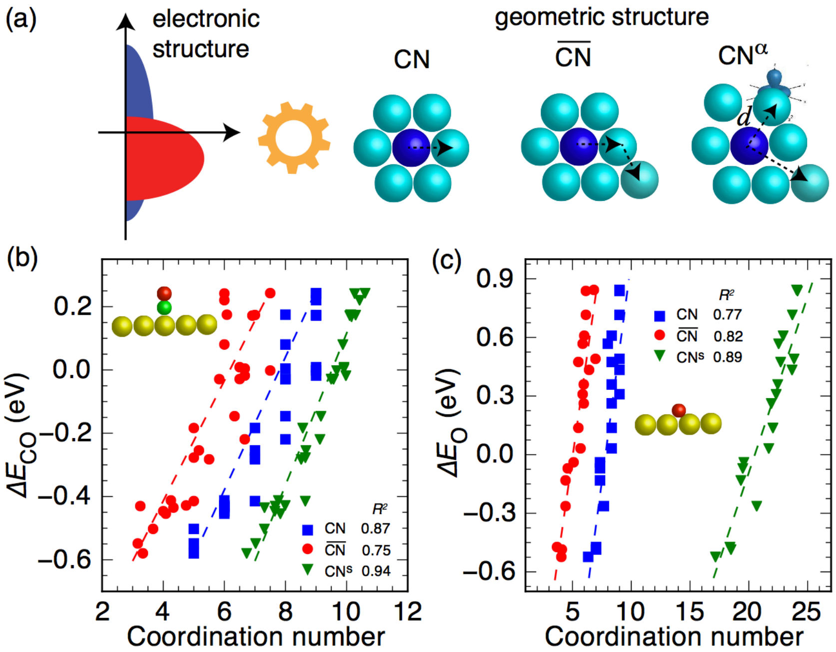

Figure 2.1: (a) Linking the electronic structure of a surface metal site to its coordination number descriptors. (b) and (c) show the correlations of coordination numbers with adsorption energies of *CO and *O at an atop and a hollow site of Au nanoparticles, respectively.

$$CN_i^\alpha = \frac{M_{2,i}^\alpha}{(t_{nn}^{\alpha,\infty})^2} = \frac{\sum_j^{r_{ij}<r_c}\left(t_{ij}^\alpha\right)^2}{(t_{nn}^{\alpha,\infty})^2},\ \alpha = s, d, \cdots .$$

In Eq. 2.3, $\left(t_{ij}^\alpha\right)^2$ is the sum of the square of the two-center one-electron hopping integral from the α-orbital of a target atom i to all relevant valence orbitals of the atom j in a given system and $(t_{nn}^{\alpha,\infty})^2$ is the corresponding value of two nearest-neighbor atoms in the fully-optimized bulk. r_c is the cutoff radius for the summation, taken as 5.5 Å. Since d-orbitals of metallic Au atoms are very low in energies, the adsorbate-surface interactions are mainly determined by *sp*-states. As shown in Fig. 2.1(b) and (c), the *s*-orbital coordination number CN^s linearly correlates with *CO and *O adsorption energies at atop and hollow sites of Au nanoparticles, respectively. We attributed the improved correlation using CN^α to explicit consideration of the symmetry of interacting orbitals and bond distances of surface atoms.

2.3.2 Microkinetic Model

To understand the effects of Au particle size in catalyzing CO oxidation, we use microkinetic models interfaced with the CATMAP[19] to map out catalytic activity onto *CO and *O adsorption energies (termed *descriptors*), see Fig. 2.2. In the microkinetic model, we include both the direct O_2 dissociation and *CO assisted O_2 activation pathways[15]. We consider four types of active sites in parameter reduction using scaling relations, e.g., (111) terrace, (100) terrace, (211) edge, and (532) kink, as shown in insets of Fig. 2.2. This reduction in kinetic parameter space is made possible by virtue of linear scaling relations[20] among adsorption energies of reaction intermediates and transition states with that of *CO or *O. For example, the formation energies of $*O_2$ and ‡O-O are linearly scaled with that of *O, while the formation energies of ‡O-CO and ‡O-O-

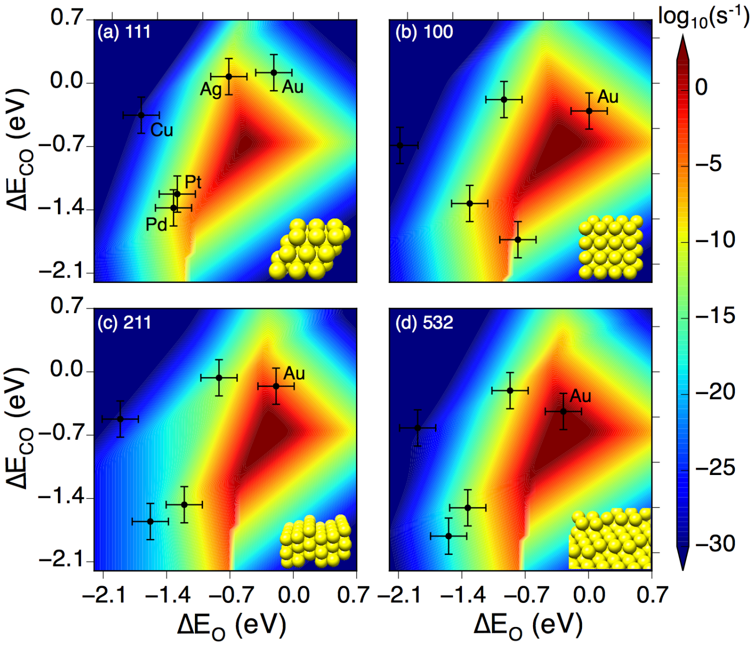

Figure 2.2: Microkinetic analysis of CO oxidation on extended Au surfaces (a) (111), (b) (100), (c) (211), and (d) (532). Insets show the surface structure of DFT models.

CO are linear combination of that of *CO and *O because those intermediates or transition states are bonded to the surface via both C and O atoms. For active metals, e.g., Pt, the direct dissociation pathway is dominant, while on less active metals, e.g., Au, the *CO assisted O_2 activation contributes the most to activity. In this analysis, we assume the interaction between adsorbed species is negligible, i.e., the coverage is very low. This is reasonable for the weakly binding region, while in the strongly binding region, e.g., Pt surfaces and Au clusters[21, 22], the reaction rate predicted here represents a lower bound[23].

2.3.3 First-principles-based embedded atom method (EAM)

To accurately predict the *CO and *O adsorption energies on a broad range of Au metal nanoparticles, we use the structure-reactivity models in Fig. 2.1. To take into account geometric strain of surface atoms due to broken bonds, we develop the embedded-atom method potential of Au trained with a limited number of DFT-GGA energies. The EAM total energy of an N-atom system can be defined as the sum of embedding energies (F_i), i.e., the energy to embed an atom i in the host electronic density (ρ_i) of the surrounding atoms, and the pairwise interaction energies (ϕ_{ij}) at interatomic distance R_{ij} between atoms i and j, see Eq. 2.3:

$$E_{tot} = \sum_{i=1}^{N} F_i(\rho_i) + \sum_{i=1}^{N} \sum_{j>i} \phi_{ij}(R_{ij}). \tag{2.3}$$

Various functional forms have been proposed to describe the embedding energy and the pairwise interaction energy. We used the formalism developed by Daw *et al.*[24]. Optimization of the parameters is performed using the downhill simplex algorithm and the cost function to be optimized is the sum of the norms of the residual differences between DFT and EAM cohesive energies of a set of bulk, surface, and nanocluster geometries[25]. The optimized parameters are provided in the Table 3.1. The python script to generate the eam.alloy

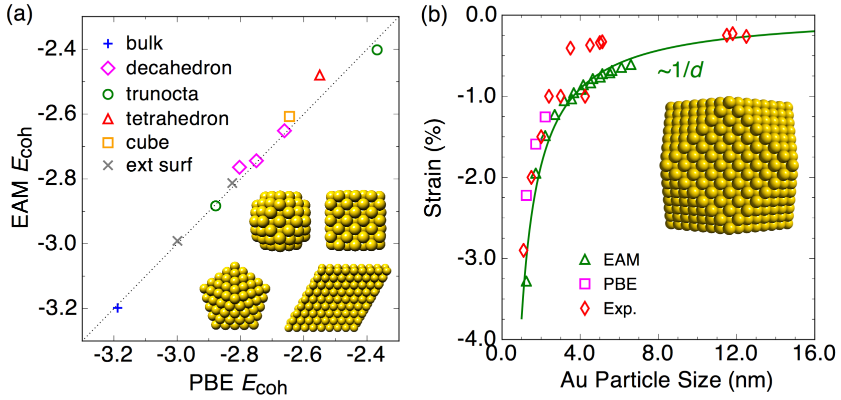

Figure 2.3: (a) Cohesive energies of Au nanoparticles (not in the training set) from EAM potential optimization vs. that from GGA-PBE calculations. (b) Geometric strain of Au metal nanoparticles from EAM potentials, compared to the GGA-PBE functional and experimental measurements.

potential file for EAM calculations in Atomic Simulation Environment (ASE) [26] can be found in literature [27]. To test predictive capability of the EAM potential for cohesive energies of new systems that are not used in training, we have shown in Fig. 2.3(a) the cohesive energies of randomly-picked EAM-optimized structures vs. that from DFT-GGA optimization. The parity plot illustrates that the cohesive energies of Au nanoparticles can be equivalently derived from EAM calculations rather than expensive GGA-PBE calculations. Figure 2.3(b) shows the interatomic strain defined as the average of surface atoms of Au nanoparticles as a function of particle size. We can see that the EAM-optimized Au nanoparticles have similar geometric strain compared to PBE-optimized structures ($<$ 201 atoms) and experimental measurements of nanoparticles up to 13 nm[28, 29, 30, 31]. Those benchmark calculations have demonstrated that the EAM potential optimized with *ab-initio* energies is sufficiently accurate for describing energy and geometric structure of a broad size range of Au nanoparticles.

2.3.4 Size effect of Au nanoparticles toward CO oxidation

We can use EAM methods for modeling thousands of metal atoms on a single- processor computer. It gives the power of predicting geometric structures of a whole range of metal

Table 2.1: Embedded atom method potential parameters for Au trained with DFT GGA-PBE energies.

r_e	2.9566	η	1.3071	F_{n0}	-2.3842
f_e	1.5292	A	0.2129	F_{n1}	-0.4126
ρ_e	20.1835	B	0.3163	F_{n2}	1.0258
ρ_m	0.7073	F_e	-2.4240	F_{n3}	-2.9954
α	9.0571	F_{m0}	-2.2719	F_0	-2.4221
β	5.4686	F_{m1}	-0.8405	F_1	0.0000
κ	0.4315	F_{m2}	1.7548	F_2	1.8160
λ	0.8642	F_{m2}	0.3234	F_3	0.8806

∗ r_e unit is Å. f_e, ρ_e, and ρ_m units are $e^-/Å^3$. A, B, F_e, F_{mi}, F_{ni} and F_i (i=0, 1, 2, 3) units are eV. Others parameters are unitless.

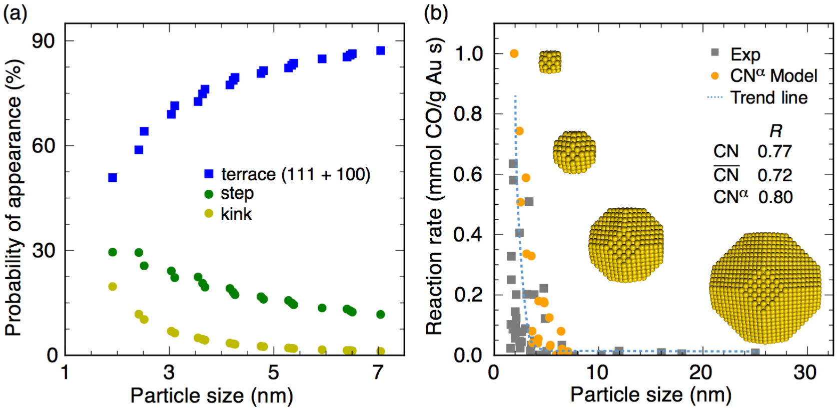

Figure 2.4: (a) Site population analysis of terrace and undercoordinated surface atoms of Wulff-constructed Au nanoparticles. (b) Experimental measured catalytic CO oxidation rates of supported Au nanocatalysts on irreducible metal oxides as a function of the size of metal nanoparticles. Model prediction based on the orbitalwise coordination number of EAM-optimized nanoparticles and volcano activity are shown to capture size effects of metal nanocatalysts.

nanoparticles and understanding its effect on catalytic performance. We optimize the geometry structure of a range of Wulff-constructed Au nanoparticles with EAM methods and then use CN, $\overline{CN}$, and CN^α to predict *CO and *O adsorption energies on all Au surface atoms/sites. We categorized the surface sites into those types as shown in Fig. 2.2. As *CO and *O adsorption energies of an atom/site are calculated using the structure-reactivity models, its effective reaction rate will be directly interpolated from the volcano activity plots in Fig. 2.2. Since *O is adsorbed at a hollow site, the reaction rate associated with a surface atom is calculated by averaging over all neighboring hollow-site configurations. After getting the catalytic rate for each surface atom of pure nanoparticles, we sum up these rates and get the average catalytic rate of this nanoparticle. As shown in Fig. 2.4(a), when it goes to larger particle size, the population of terrace sites increases while that of the under-coordinated surface atoms (step and kink) decreases dramatically. With the activity trend from microkinetic analysis in Fig. 2.2, such decrease of under-coordinated atoms would result in smaller catalytic activity. The correlation between the estimated CO oxidation rate vs. the particle size together with measured rates from literature[17] over a broad range of metal oxide supports is shown in Fig. 2.4(b). We can see that such a simple CN^{α}-activity model without considering metal-support interactions and effects of gas phase species on the equilibrium shape of metal nanoparticles[32] can predict general activity trend of Au nanocatalysts with respect to particle size. Model analysis has shown that the orbitalwise coordination number shows similar performance compared to the regular CN and generalized $\overline{CN}$ coordination numbers for predicting activity trends, which indicates the insensitivity of surface strains in structure-activity models. With coordination-based descriptors, the approach statistically illustrates the importance of under-coordinated atoms in understanding size effects of Au-catalyzed CO oxidation.

2.4 Conclusion

In summary, we have developed an approach to a priori estimation of catalytic activity of metal nanoparticles using coordination-based reactivity descriptors and microkinetic analysis of complex reaction pathways. First-principles based EAM potentials are developed for geometry optimization of large nanoparticles. The method proposed can be used for predicting optimize size and shape of metal nanoparticles for any particular reaction. The extension of coordination number based descriptors with kinetic analysis to multimetallics and interfacial sites of supported metal nanoparticles is in progress.

Chapter 3

Overcoming Site Heterogeneity In Search of Metal Nanocatalysts

3.1 Introduction

Transition metal clusters or nanoparticles are ubiquitous in heterogeneous catalysis. Developing methods for an accurate prediction of reaction activity trends of nanocatalysts with diverse structural characteristics, *e.g.*, size, shape, composition, and ordering, is one of the major goals in catalytic science and remains as a grand challenge toward *in-silico* catalyst design.[17, 33, 34, 35] Traditionally, the catalytic properties of metal nanoparticles were treated by the periodic density functional theory (DFT) approach on a facet-by-facet basis.[15, 36, 37, 38, 39, 40, 41] With adsorption-energy scaling relations, the catalytic outcome of a complex reaction at metal nanocatalysts can be mapped onto one or two reactivity descriptors, *e.g.*, energetics of simple adsorbates.[15, 19, 27, 42] Such a catalyst design approach is extremely useful for understanding catalytic activity trends of model surfaces and has been guiding catalyst discovery since its early development.[43, 44, 45, 46]

To address the challenge of site heterogeneity of metal nanocatalysts, there have been great efforts in developing models relating the structure of an active site to reactivity descriptors. Arguably, the *d*-band chemisorption theory developed by Hammer and Nørskov[47] is one of the most often used model for understanding the catalytic function of transition metals.

However, electronic descriptors are not easy to implement in practice due to the complex dependence of surface reactivity on the geometric strain and metal ligand.[37, 48] Calle-Vallejo *et al.* have popularized the concept of coordination-based descriptors and proposed the generalized coordination numbers $\overline{CN}$ in introducing structure sensitivity to scaling relations and designing Pt cavity sites with improved oxygen reduction activity.[16, 36, 49]

Recently, the orbitalwise coordination numbers CN^{α} with an explicit consideration of the geometric strain and metal ligand of an active site have been shown to predict the reactivity properties of coinage metals and their alloys,[11] and capture intrinsic size effects in Au-catalyzed CO oxidation.[27] Inspired by this concept, we develop an approach to modeling catalytic activity of metal nanoparticles that effectively takes into account heterogeneity of surface sites. Compared to the electronic descriptors, *e.g.*, *d*-band center ϵ_d, the CN^{α} is physically intuitive and can be computed in a similar way as the $\overline{CN}$.[11] Using oxygen reduction reaction (ORR) as an example,[44] we demonstrate that the approach captures the activity trend of pure Pt nanoparticles ($\sim$1$-$7 nm) toward oxygen reduction and suggests several Pt monolayer core-shell nanoalloys with enhanced ORR activity and reduced cost.

3.2 Computational details

All DFT calculations about Pt systems were performed by QUICKSTEP in CP2K package [50]. The exchange-correlation potential was treated with the generalized gradient approximation parameterized by the spin-polarized revised Perdew-Burke-Ernzerh (GGA-RPBE) functional [51, 52]. The wavefunctions were expanded in molecular optimized short range double-ζ valence polarized Gaussian basis sets (DZVP-MOLOPT-SR-GTH) for all metal elements, while molecular optimized triple-ζ valence polarized Gaussian basis sets (TZVP-MOLOPT-GTH) for all adsorbates, with an auxiliary plane-wave basis set with a cutoff energy of 320 Ry. Core electrons have been modeled by the scalar relativistic norm-conserving Goedecker-Teter-Hutter (GTH) potentials [53] with 1, 6, and 10 valence electrons for H, O, and Pt, respectively. In the geometry optimizations, the maximum forces were converged to 0.1 eV/Å. The standard hydrogen electrode is used for relating the free energy of the (H^+ + e^-) pair to that of gas phase H_2 [44]. The adsorption energies of OH and OOH were calculated as the difference between the electronic energy of the adsorbate-nanoparticle/slab complex and the sum of the electronic energies of the bare system and gas phase H_2O and H_2:

$$\Delta E_{*OH} = E_{*OH} - (E_{*} + E_{H_2O} - E_{H_2}/2).$$

$$\Delta E_{*OOH} = E_{*OOH} - (E_{*} + 2 * E_{H_2O} - E_{H_2}).$$

Where E_{*OH}, E_{*OOH}, E_{*}, E_{H_2O}, and E_{H_2} are electronic energies of the adsorbate-nanoparticle/slab complex, the bare nanoparticle/slab, gas phase H_2O and H_2 molecules. Zero point energy corrections and entropic contributions to the free energies were taken from ref [49] and we assume these values don't change across metal surfaces under consideration [43]. The solvation energy of adsorbed species (*OH: −0.6 eV, *OOH: −0.3 eV) is also approximated to be constant [44].

To predict the mass activity of metal nanoparticles, we first calculated the Gibbs free formation energy of *OH and *OOH intermediates at a given site using:

$$\Delta G_{*\mathrm{OH}} = 0.17CN^{s} - 1.33 \tag{3.1}$$

$$\Delta G_{*\mathrm{OOH}} = 0.17CN^{s} + 1.87 \tag{3.2}$$

We then follow the literature [46] for computing activity relative to Pt(111) which is limited by *OH removal and has $\Delta G_{\mathrm{OH},Pt_{111}} = 0.79$ and $\Delta G_{OOH,Pt_{111}} = 3.99$. For the O_2 activation step, the activity is calculated by:

$$\begin{aligned}
A1 &= k_B T ln(j/j_{Pt_{111}}) \\
&= (\Delta G_{r_4,Pt_{111}} - \Delta G_{r_1}) \\
&= (\Delta G_{\mathrm{H_2O}} - \Delta G_{\mathrm{OH},Pt_{111}}) - (\Delta G_{^*\mathrm{OOH}} - \Delta G_{O_2}) \\
&= (\Delta G_{\mathrm{H_2O}} - \Delta G_{\mathrm{OH},Pt_{111}}) - (\Delta G_{^*\mathrm{OOH}} - \Delta G_{OOH,Pt_{111}}) - (\Delta G_{OOH,Pt_{111}} - \Delta G_{\mathrm{O_2}}) \\
&= 0.136 - (\Delta G_{^*\mathrm{OOH}} - \Delta G_{OOH,Pt_{111}}) \qquad (3.3)
\end{aligned}$$

For the *OH removal step, the activity is calculated by:

$$\begin{aligned}
A4 &= k_B T ln(j/j_{Pt_{111}}) \\
&= \Delta G_{r_4,Pt_{111}} - \Delta G_{r_4} \\
&= \Delta G_{^*\mathrm{OH}} - \Delta G_{\mathrm{OH},Pt_{111}} \qquad (3.4)
\end{aligned}$$

Then, the activity of the site is taken as the minima of A1 and A4. The total rate relative to that of Pt(111) is simply calculated as a summation of all surface sites: TotalRate = $\sum \exp \frac{A}{k_B T}$. The mass activity of the particle is obtained by dividing the TotalRate by the number of atoms in the whole particle.

3.3 Results and discussion

3.3.1 Site heterogeneity of Pt nanoparticles toward oxygen reduction

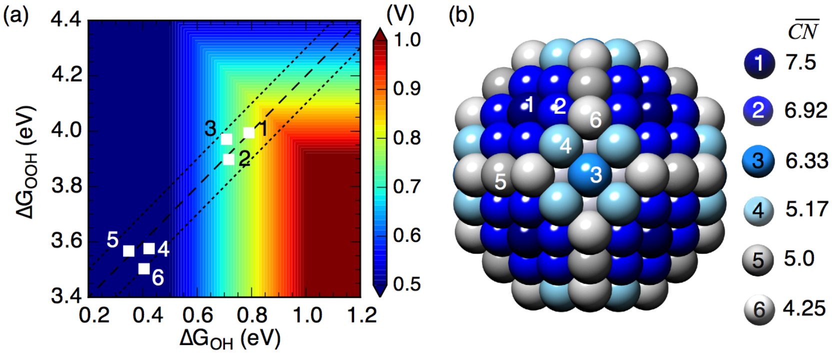

Figure 3.1: ORR activity map of metal nanocatalysts. (a) Theoretical ORR limiting potential as a function of *OH and *OOH free formation energies. (b) Variations in the coordination environment of surface sites of a Pt_{201} nanoparticle quantified by the generalized coordination number $\overline{CN}$. Surface sites (1−6) are positioned on the activity map using DFT-calculated *OH and *OOH energies.

Because of the sluggish kinetics of the oxygen reduction reaction (ORR) at the fuel cell cathode, the state-of-the-art elemental metal electrocatalyst, containing Platinum (Pt) nanoparticles (<5 nm), sacrifices ∼300 mV potential for appreciable current densities.[43] Driven by a limited supply of Pt and its high price, a decades-long search for high-performance Pt nanoalloys[54] and non-precious metal alternatives[55, 56, 57, 58] with an increasing arsenal of experimental and computational tools is still an ongoing task. At typical operating potentials (∼0.9 V vs. RHE), oxygen reduction on Pt follows the associative mechanism,[39, 44, 59, 60] where the *OOH formation from O_2 activation and *OH removal to release active sites are potentially rate limiting depending on the nature of an active site.[46] Figure **??**(a) maps out the theoretical ORR limiting potential as a function of *OH and *OOH free formation energies, assuming that the thermodynamic stability of *OH and *OOH is independent of each other. The theoretical limiting potential of ORR is defined as the cathodic potential at which all elementary steps are exergonic.[44] The DFT energies reported here were calculated using the generalized gradient approximation (GGA-RPBE) with GTH pseudopotentials implemented in CP2K.[61] The standard hydrogen electrode is used for relating the free energy of the $(H^+ + e^-)$ pair to that of gas phase H_2.[44] Zero point energy corrections and entropic contributions to the free energies were taken from ref[49] and we assume these values don't change across metal surfaces under consideration.[43] The solvation energy of adsorbed species (*OH: −0.6 eV, *OOH: −0.3 eV) is also approximated to be constant.[44] To illustrate the site heterogeneity of metal nanocatalysts, we show in Fig. **??**(b) a 201-atoms nanoparticle with color-coded surface atoms quantified by the regular and generalized coordination numbers, CN and $\overline{CN}$, respectively. The DFT-calculated free formation energies of *OH and *OOH on various surface sites (1−6) are overlaid on the activity volcano. As we can see, there is a strong linear correlation between *OH and *OOH free formation energy for various Pt sites, approximately $\Delta G_{*\mathrm{OOH}} = \Delta G_{*\mathrm{OH}} + 3.2$ ± 0.1 eV. The same correlation has been shown to be valid on metal surfaces, metal oxides, etc, which drastically limits the attainable catalytic activity according to the Sabatier principle.[49, 62, 63, 64, 65]

3.3.2 Orbitalwise coordination numbers as reactivity descriptors

To design Pt nanocatalysts with improved performance, an intuitive descriptor that accurately predicts adsorption properties of metal sites is essential. Following the same line of previous studies,[11, 18, 27, 66] we show in Fig. 3.2 (a) the linear correlations of the s-orbital based coordination number CN^s with the *OH

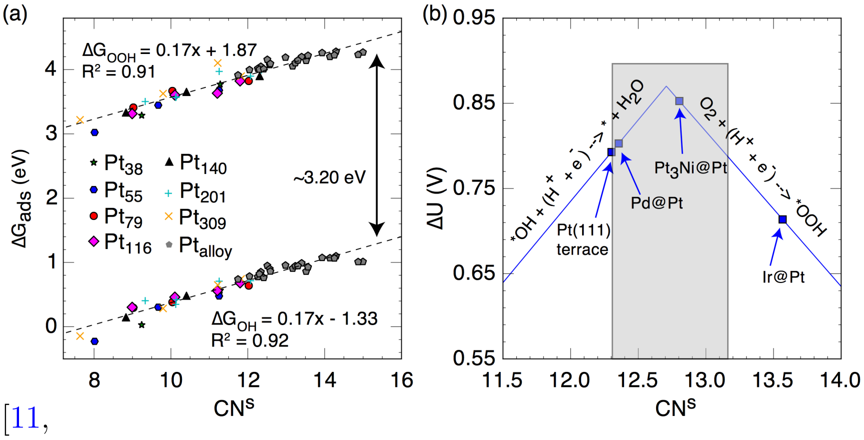

Figure 3.2: Orbitalwise coordination number as an activity descriptor. (a) *OH and *OOH free formation energies and (b) theoretical ORR limiting potential at surface sites of Pt nanoparticles described by the s-orbital based coordination number CN^s. A few model alloys with known ORR activity are located on the volcano plot based on the CN^s of the (111) terrace site of the 314-atoms Pt nanoalloys, illustrating the predictive power of the model.

and *OOH free formation energies at various Pt sites. A broad range of Pt nanoparticles and Pt monolayer core-shell nanoparticles are used in the regression model. For Pt alloys, we include Pt_{116}, Pt_{140}, and Pt_{201} nanoparticles with varying transition metals (Ni, Pd, Pt, Co, Rh, Ir, and Ru) in the core. Coinage metals (Cu, Ag, and Au) are not included because of their distinct properties from Pt, which somehow delineates the correlation, see Fig. 3.3. Compared to the regular and generalized coordination numbers,[16] the orbitalwise coordination number exhibits an universal linear correlation with the surface reactivity of pure Pt nanoparticles and nanoalloys. The s-orbital based coordination number CN^s ($R^2 \sim 0.91$) outperforms the d-orbital based counterpart CN^d ($R^2 \sim 0.84$), see Fig. 3.4. The origin of this phenomenon deserves a separate investigation, and it is out of the scope of the current study. This observation supports the important role of sp-electrons in governing the adsorption strength of *OH and *OOH at Pt sites, which is in line with previous studies of *OH adsorption on Pt and Pd near surface alloys[67]. For *OH or *OOH adsorption at Pt sites, the interaction of adsorbate valence orbitals with the jellium-like substrate sp-states gives broadened resonance states at lower energies. This normalized resonance state further interacts with localized d-states giving rise to bonding and anti-bonding orbitals. Although the fine features of adsorbate density of states are introduced by interactions with d-states, the hybridization energy is relatively small because of the almost fully occupied adsorbate-metal anti-bonding states.[67, 68]

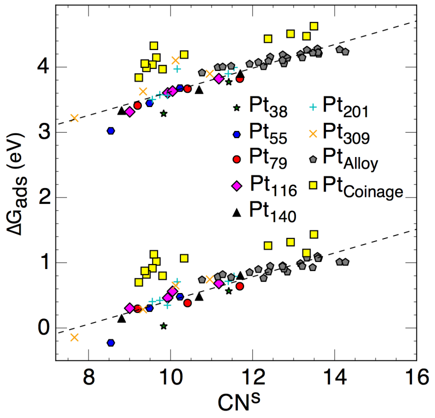

Figure 3.3: The linear correlations of the s-orbital based coordination number CN^s with the *OH and *OOH free formation energies at various Pt sites including coinage metals in the core.

Since *OH and *OOH free formation energies $\Delta G_{*\mathrm{OH}}$ and $\Delta G_{*\mathrm{OOH}}$ are linearly correlated with CN^s, we can use CN^s as a single descriptor of the ORR activity at Pt sites.

In Fig. 3.2(b), we develop the structure-activity relationship between the theoretical ORR limiting potential and CN^s. We calculate the corresponding equilibrium potential of O_2 activation and *OH removal steps using the correlations of $\Delta G_{*\mathrm{OH}}$ and $\Delta G_{*\mathrm{OOH}}$ with the CN^s. For O_2 activation and *OH removal steps, we have $U_1 = -(\Delta G_{*\mathrm{OOH}} - \Delta G_{\mathrm{O}_2})/nF = -0.17CN^s - 1.87 + 4.92$ and $U_2 = -(0 - \Delta G_{*\mathrm{OH}})/nF = 0.17CN^s - 1.33$, respectively, where n is the number of electrons transferred in this step and F is the Faraday's constant. The limiting potential of ORR is defined as the minimal potential at which all elementary steps are exergonic in free energy, i.e., $U = min(U_1, U_2)$, as illustrated in the Fig. 3.2(b).

On the left side of the volcano plot, the potential limiting step is *OH removal to release active sites while on the right side O_2 activation forming *OOH is kinetically slow. The (111)-terminated terrace site of large nanoparticles is located on the left side of the volcano plot with a limiting potential ∼0.8 V vs. RHE, consistent with previous DFT calculations.[44] This volcano plot is analogous to the structure-activity relationship developed by Calle-Vallejo *et al.* using the generalized coordination numbers $\overline{CN}$. They both suggest that slightly increasing the coordination number relative to that of (111)-terminated terrace sites will reduce the overpotential by weakening the *OH adsorption, thus pushing ORR activity toward the top of the volcano.[49] Since the CN^s is physically intuitive and contains the information about the local geometric strain and metal ligand, this can be envisioned, as shown in Fig. 3.2(b), by depositing a Pt monolayer on (111)-terminated single-crystal surfaces with a smaller interatomic spacing d, *e.g.*, Pd@Pt_{ML}

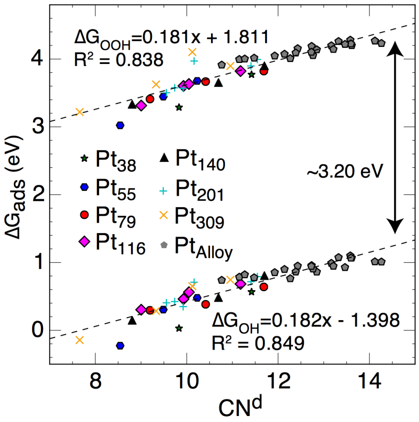

Figure 3.4: *OH and *OOH free formation energies using the d-orbital based CN^d as an activity descriptor.

and $Pt_3Ni@Pt_{ML}$. Noteworthily, $Ir@Pt_{ML}$ gives over-coordinated surface sites because of a compressive strain (smaller d) and a more extended Ir d-orbital (larger r_d), both leading to a larger coordination number because of $CN^s \propto r_d^{3/2}/d^{7/2}$.[11, 37] The predicted ORR activity trend shown in Fig. 3.2(b) is consistent with experimental measurements,[45] justifying the approach to designing new Pt nanocatalysts.

3.3.3 Size effect of Pt nanoparticles toward oxygen reduction

The structure-activity correlation in Fig. 3.2(b) allows us to explore size effects of Pt nanoparticles in catalyzing oxygen reduction. We first developed the *ab-initio* EAM potential using a number of DFT-GGA energies of Pt nanoparticles and bulk systems, following the formalism of the EAM potential developed previously [24]. The optimized EAM potential parameters are shown in Table 2.1. This type of *ab-initio* EAM potentials have been shown to capture geometric structures of metal nanoparticles [27], see Fig. 3.5.

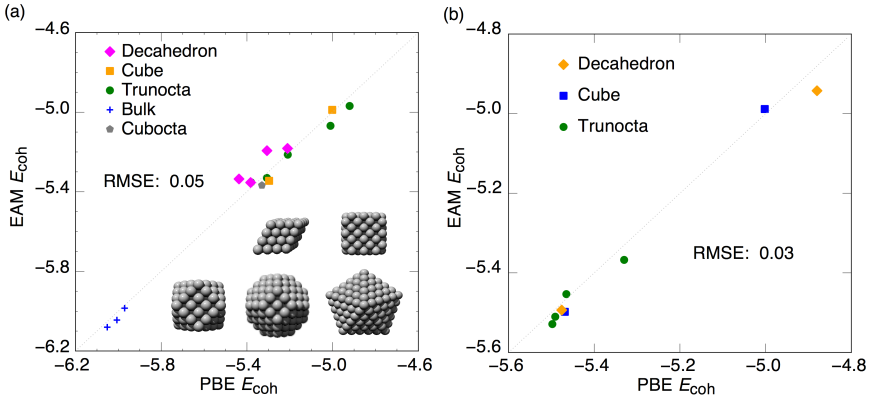

Figure 3.5: Cohesive energies of Pt nanoparticles from the *ab-initio* EAM potential vs. that from GGA-PBE calculations in (a) training, (b) test.

We optimized the Wulff-constructed Pt nanoparticles up to 7 nm using the tabulated potential parameters. An electrokinetic model is used for predicting the reaction rate of any given Pt site relative to Pt(111) [46], where the unity transfer coefficient is used [69, 70].

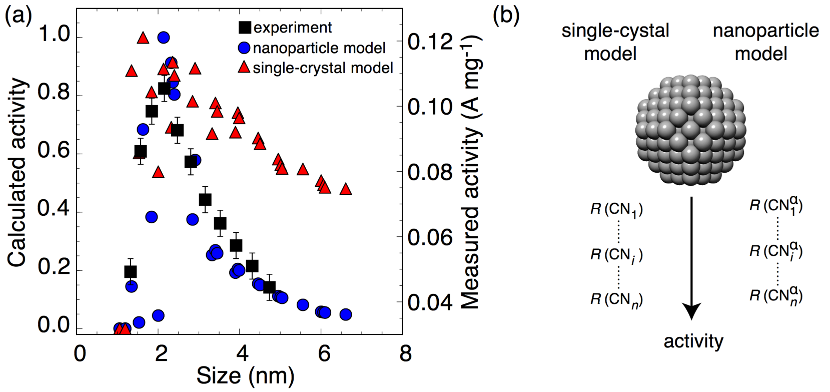

Figure 3.6: Size effects of Pt nanoparticles toward oxygen reduction. (a) Model predicted vs. measured mass activity of Pt nanoparticles for oxygen reduction. The predicted activity is normalized using the highest mass activity. The *ab-initio* EAM potential was used for optimizing the geometric structures of a series of Wulff-constructed Pt nanoparticles. (b) Schematics of the nanoparticle model developed herein with the orbitalwise CN^{α} and the single-crystal model with the regular CN for predicting activity of metal nanocatalysts.

The activity of a given Pt nanoparticle can then be estimated by a sum of the rate of individual surface sites by leveraging a fast computation of the CN^s of all surface atoms. From Fig. 3.1, we can see that the (111)-terminated terrace site has a higher ORR activity than the under-coordinated step, edge, and kink sites at which *OH adsorption is too strong. As the particle size goes larger, the number of more active (111) terrace site increases, giving higher activity; however, the population of surface Pt atoms relative to the bulk is decreasing with particle size, resulting in an optimal mass activity at ∼2.2 nm, in excellent agreement with experimental measurements [69]. In contrast to our nanoparticle model with the CN^{α}, as illustrated in Fig. 3.6(b), the traditional single-crystal model using DFT-calculated *OH and *OOH energies on a few types of facets including (111), (211), (100), and (532) does not capture the s of the ORR activity trend with respect to the particle size. It overestimates the reactivity at larger sizes because of using central terrace atoms which have higher activity compared to sites close to the edges or corners.

$*$ r_e unit is Å. f_e, ρ_e, and ρ_m units are e$^-$/Å^3. A, B, F_e, F_{mi}, F_{ni} and F_i (i=0, 1, 2, 3) units are eV. Others parameters are unitless.

Table 3.1: Embedded atom method potential parameters for Pt trained with DFT GGA-PBE energies.

r_e	2.8324	η	1.3622	F_{n0}	−4.1361
f_e	2.3365	A	0.4381	F_{n1}	−0.4670
ρ_e	31.9479	B	0.6828	F_{n2}	0.6076
ρ_m	0.8400	F_e	−4.1927	F_{n3}	0.3778
α	8.7916	F_{m0}	−4.1305	F_0	−4.1847
β	4.7183	F_{m1}	−0.4755	F_1	0.0000
κ	0.3655	F_{m2}	0.5804	F_2	2.8221
λ	0.7466	F_{m3}	−3.0746	F_3	4.4024

3.3.4 Rapid screening of $A_3B@Pt_{ML}$ nanocatalysts

To further improve catalytic activity of Pt nanoparticles and reduce catalyst cost, we are applying the approach to an extensive search of Pt nanoalloys. We chose the truncated octahedral nanoparticle with 314 atoms as the model, which is close to the optimal size (∼2.2 nm) of pure Pt nanoparticles in Fig. 3.6. We have performed self-consistent DFT calculations at the GGA-RPBE level to optimize the alloy nanoparticles ($A_3B@Pt_{ML}$) in a wide range of metal combinations of

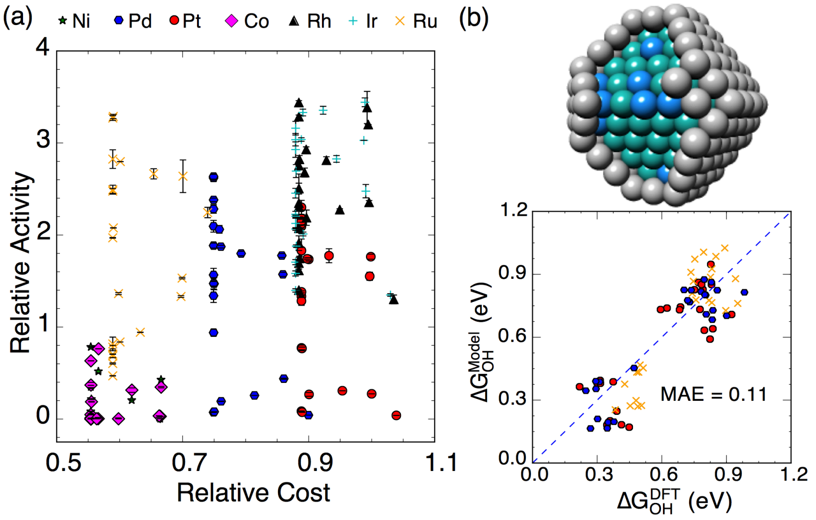

Figure 3.7: (a) Rapid screening of Pt monolayer core-shell nanoalloys $A_3B@Pt_{ML}$ using the orbitalwise coordination number CN^s as a descriptor. 314-atoms nanoparticles with a 3:1 A:B ratio at the core were used (see the inset structural model). The activity is relative to Pt(111). The average activity and standard deviation of 5 random configurations in the core are reported. (b) Validation of model-predicted *OH free formation energies at identified alloys (5 sites for 5 core-randomalized alloys were used for $Ru_3Ta@Pt_{ML}$, $Pd_3Cu@Pt_{ML}$, and $Pt_3Ni@Pt_{ML}$).

A and B, where A represents fcc metals (Ni, Pd, Pt, Co, Rh, Ir, and Ru) and B represents all transition and noble metals across the periodic table. Here we chose the 1^{st} generation core-shell nanoalloys with a surface Pt monolayer because this type of alloys has been extensively employed in fuel cell catalysis.[71, 72] Electrochemical techniques can be used to control the composition in the core and deposit a Pt monolayer on the top.[72, 73, 74, 75] We use the orbitalwise CN^s as a descriptor for rapid prediction of total activity of Pt nanoalloys toward oxygen reduction. For a given composition, 5 random alloys[76, 77] are created in the core with A:B at 3:1 ratio and the average activity is reported. By varying the constituent metals in alloy cores, we can rapidly explore the chemical space of this type of Pt nanoalloys. In Fig. 3.7, we are showing the predicted ORR activity and the corresponding metal cost for Pt monolayer core-shell nanoalloys. The cost of alloys only serves as a rough estimation based on the current prices of constituent metals since metal precursors are actually used in synthesis. We can see that lots of alloy systems exhibit improved catalytic activity compared to pure Pt nanoparticles and have reduced cost, including the previously observed[72] $Pt_3Ni@Pt_{ML}$ and others to be synthesized, e.g., $Ru_3X@Pt_{ML}$ (X: Ta, Nb, Pt, Pd, and Mo) and $Pd_3X@Pt_{ML}$ (X: Cu, Mn, Cr, and Re). Self-consistent DFT calculations of *OH adsorption on three identified alloys were used to validate the prediction ($Ru_3Ta@Pt_{ML}$, $Pd_3Cu@Pt_{ML}$, and $Pt_3Ni@Pt_{ML}$ with the structures provided in the SI). Figure 3.7(b) showed that the model-predicted *OH free formation energies at surface sites of 5 core-randomized alloys agree with DFT calculations with MAE∼0.11 eV. The approach developed here is fast and highly accurate in predicting optimal composition and structure of Pt nanoalloys, thus effectively tackling the site heterogeneity of metal nanocatalysts.

3.4 Conclusion

To conclude, we develop a new approach to predicting catalytic activity trends of metal nanoparticles *in priori*, aiming to overcome the challenge of site heterogeneity introduced by the geometric strain and metal ligand of an active site. Using oxygen reduction as an example, we show that the structure-activity relationship with the orbitalwise coordination number CN^{α} allows us to semi-quantitatively understand size effects of Pt nanocatalysts. More importantly, large-scale materials screening enabled by the approach validates several previously identified ORR alloy catalysts and suggests several Pt monolayer core-shell nanoalloys with potentially improved ORR activity and reduced cost. The approach presented here facilitates a transition from traditional single-crystal models to nanoparticles in theory-guided catalyst discovery.

Chapter 4

Bayesian Model of Chemisorption for Adsorbate-Specific Tuning of Electrocatalysis

4.1 Introduction

The adsorption of molecules or their fragments at surfaces is a fundamental process for many technological applications, such as self-assembled molecular coatings, corrosion protection, chemical sensing, and catalysis [78]. Due to the interplay of orbital hybridization and electron transfer, the chemisorption phenomenon can be formidably complex. With recent advances in electron microscopy and spectroscopy techniques which promise to reveal the orbital-level information of adsorption complexes, a number of chemisorption models have emerged [14, 37, 67, 79, 80, 81, 82, 83, 84, 85, 86, 87, 88]. Among those the *d*-band model, developed by Hammer and Nørskov [14, 79, 80], was widely used for describing chemical bonding at metal surfaces [48, 89, 90] and to some extent their compounds. It relates the electronic structure of an active metal site, i.e., the average energy of *d*-states relative to the Fermi level (*d*-band center), to the local chemical reactivity. Since all *d*-block metals have a broad and featureless *sp*-band, the main difference in adsorption energies comes from the metal-specific interactions of an adsorbate with substrate *d*-states. In general, a metal site with a higher (lower) *d*-band center leads to higher (lower) energies of adsorbate-metal anti-bonding states. As a consequence, the filling of those unfavorable states will be decreased (increased), which results in stronger (weaker) chemisorption. This simple rule has proven to be useful in search of improved catalysts in many chemical and electrochemical reactions [91, 92].

However, exceptions to this simple rule exist, where the higher (lower) *d*-band center is not associated with stronger (weaker) chemisorption. Those outliers can often be rationalized on a case-by-case basis by considering some other characteristics of electronic structures, such as the orbital orthogonalization energy or Pauli repulsion [37, 67], the shape of the *d*-states distribution [88], or the interatomic coupling of discrete energy levels in nanoclusters [11]. Developing a predictive model of chemisorption that considers the detailed electronic structure of an active site represents one of the long-term goals of this project. This motivates us to develop a general model by employing parameterized Hamiltonians, e.g., the Anderson-type Hamiltonian. It was originally used for describing magnetic properties of impurities in a bulk metallic host [93] and extended with success by Newns, Grimley, and many others to chemisorption processes [81, 82, 83, 84, 85, 86, 87]. The approach uses a basis set of orbitals consisting of the states of an adsorbate and the substrate for second quantization and then solves the hybridization problem within the self-consistent Hartree-Fock scheme. Simply put, the model extends the basic two-level interaction picture from molecular species to solid interfaces, where an adsorbate will not just interact with one or more discrete states, but rather with a quasi-continuum of Bloch states. Despite a remarkable success in qualitatively understanding adsorption phenomena at surfaces, particularly for metals, its application in surface science and chemistry remains limited due to the lack of accurate model parameters and error estimates.

4.2 Computational Method

Bayesian learning [94] was used to infer model parameters from data. In contrast to purely data-driven models [95, 96, 97], incorporating physical models into learning, often with very limited data, is attractive. For example, it has been used for the calibration and validation of thermodynamic models for the uptake of CO_2 in mesoporous silica-supported amines [98], designing the Bayesian error estimation functional with van der Waals correlation [99], and identifying active sites and reaction mechanisms in catalysis [100]. Bayesian learning produces posterior distributions of parameters under the influence of observations and prior knowledge. The use of parameter distributions as opposed to computationally-derived deterministic values has obvious advantages for uncertainty quantification in multi-scale modeling. Inspired by those efforts, we demonstrate that by marrying the Newns-Anderson model with ab initio data in Bayes' rule [101], the Bayesian model of chemisorption can be developed for probing orbitalwise nature of adsorbate-surface interactions and prediction of reactivity trends with uncertainty quantification.

4.2.1 NewnsAndersonModel

Let's consider a surface in which electrons occupy a set of continuous states with one-electron wavefunction $|k\rangle$ of energy ϵ_k, and an atom with one valence electron of energy ϵ_a and wavefunction $|a\rangle$. Imagine that when the atom is brought to a position just outside of the surface, the two sets of states will interact. The strength of such interactions is mainly determined by interatomic coupling matrix elements $V_{ak} = \langle a|\hat{H}|k\rangle$, where $\hat{H}$ is the Hamiltonian of the system [85, 93, 102]. The Newns-Anderson-type Hamiltonian $\hat{H}$ is defined as,

$$\hat{H} = \sum_{\sigma} \Big\{ \epsilon_{a\sigma} n_{a\sigma} + \sum_{k} \epsilon_k n_{k\sigma} + \sum_{k} (V_{ak} c^{\dagger}_{k\sigma} c_{a\sigma} + V^{*}_{ka} c^{\dagger}_{a\sigma} c_{k\sigma}) \Big\}, \tag{4.1}$$

where σ denotes the electron spin, n is the orbital occupancy operator, and $c^\dagger$ and c represent the creation and annihilation operator, respectively. The first two terms in Eq. 4.1 are the one electron energies from the adsorbate and substrate when they are infinitely separated. The last term captures the coupling, or intuitively electron hopping, between the adsorbate state $|a\rangle$ and a continuum of substrate states $|k\rangle$. Within the Hartree-Fock approximation, the effective adsorbate energy level of spin σ can be written as [84],

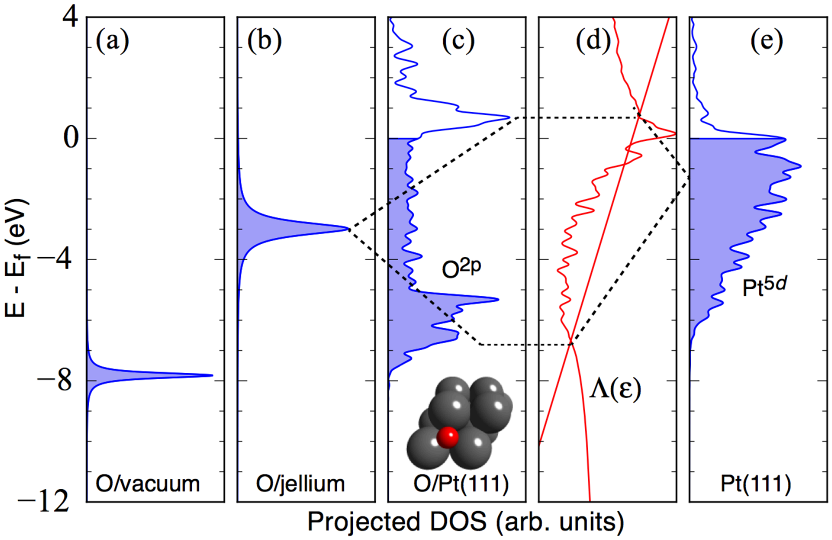

Figure 4.1: The evolution of an adsorbate state (O^{2p}) upon adsorption (a)−(e) described by the Newns-Anderson model, using *O at the hollow site of Pt(111) as an example.

$$\epsilon_{a\sigma} = \epsilon_a^0 + V_{im} + U_{eff}\langle n_{a,-\sigma}\rangle, \tag{4.2}$$

where ϵ_a^0 represents the unperturbed adsorbate energy level relative to the Fermi level of the substrate, V_{im} is the image potential due to charge polarization at interfaces, and U_{eff} is the effective intra-atomic Coulomb repulsion between electrons of opposite spin in $|a\rangle$ [84]. If we assume that the one-electron states of an adsorbed system can be described as a linear combination of the unperturbed adsorbate $|a\rangle$ and substrate $|k\rangle$ states, the one-electron Schrödinger equation can be solved using the Green's function approach [85]. The overlap matrix $S_{ak} = \langle a|k\rangle$ can be included to consider nonorthogonality of the basis set [103, 104]. The important information coming out the model is the projected density of states onto the adsorbate valence level $\rho_{a\sigma}(\epsilon)$,

$$\rho_{a\sigma}(\epsilon) = \frac{1}{\pi} \frac{\Delta(\epsilon)}{[\epsilon - (\epsilon_{a\sigma} + \Lambda(\epsilon))]^2 + \Delta(\epsilon)^2}, \tag{4.3}$$

from which the orbital occupancy $\langle n_{a,\sigma} \rangle$ can be obtained by integrating occupied states of the spin σ. In Eq. 4.3, the chemisorption function $\Delta(\epsilon)$ can be considered as the modulated density of states of the substrate, written as,

$$\Delta(\epsilon) = \pi \sum_k |\epsilon_k S_{ak} - V_{ak}|^2 \delta(\epsilon - \epsilon_k), \tag{4.4}$$

which determines the lifetime broadening of the adsorbate state. $\Lambda(\epsilon)$ in Eq. 4.3 is the Hilbert transform of $\Delta(\epsilon)$ and characterizes the shift of the adsorbate state due to electronic coupling with the substrate. $\rho_{a\sigma}(\epsilon)$ has to be computed self-consistently because $\epsilon_{a\sigma}$ explicitly depends on the occupancy of the opposite spin $\langle n_{a,-\sigma} \rangle$. The important outcome from the model is the interaction energy, which can be obtained by integrating occupied states with a proper consideration of the reference [84, 105, 106].

To put mathematical equations into visualization, in Fig. 4.1, we illustrate the chemical bonding process of an atom on a metal surface. Zero is the Fermi level. Figure 4.1(a) shows the valence state of an atom in vacuum. The interaction of the atom state with the jellium-like *sp*-states (not shown) gives a resonance state which has higher energies because of the image potential and Coulomb repulsion, see Fig. 4.1(b). This resonance state further interacts with the localized *d*-states shown in Fig. 4.1(e) giving rise to the adsorbate density of states in Fig. 4.1(c). The adsorbate line intersects with the chemisorption function $\Lambda(\epsilon)$ as shown in Fig. 4.1(d), forming the bonding and anti-bonding states. The interaction with the *sp*-band is assumed to be similar for transition-metal surfaces since they have a similar broad and featureless *sp*-band. The interaction with the localized *d*-band governs trends of surface reactivity. The model singles out two important surface properties [14]: (i) the d-band center ϵ_d, and (ii) the interatomic coupling matrix element V_{ad}.

The binding energy ΔE_{ads} between adsorbate and surface can be separated into two parts, as shown in Eq. 4.11

$$\Delta E_{ads} = \Delta E_{sp} + \Delta E_d, \tag{4.5}$$

where ΔE_{sp} is the hybridization energy due to the interaction between adsorbate energy level $\epsilon_{a\sigma}$ and sp-band of metal surface, and ΔE_d is the hybridization energy due to the interaction between adsorbate energy level $\epsilon_{a\sigma}$ and d-band of metal surface. Since all transition metals have similar wide jellium-like s-band with filling to be 0.5, we can assume ΔE_{sp} is a constant for all transition metals. To calculate ΔE_d, we consider the formula from [107, 108]:

$$\begin{aligned}\Delta E_d &= \left(\frac{2}{\pi}\int_{-\infty}^{0} \text{Arc tan}\left(\frac{\Delta(\epsilon)}{\epsilon - \epsilon_{a\sigma} - \Lambda(\epsilon)}\right) \mathrm{d}\epsilon - n_{a\sigma}\epsilon_{a\sigma}\right) - (2 * (1+f) * S_{ad} * V_{ad}) \\ &= \left(\frac{2}{\pi}\int_{-\infty}^{0} \text{Arc tan}\left(\frac{\Delta(\epsilon)}{\epsilon - \epsilon_{a\sigma} - \Lambda(\epsilon)}\right) \mathrm{d}\epsilon - n_{a\sigma}\epsilon_{a\sigma}\right) + (2 * (1+f) * \alpha * V_{ad}^2) \end{aligned} \tag{4.6}$$

where the first term is attractive if the d-band is not fully occupied and the second term is Pauli repulsion due to overlap. The constant 2 in the equation considers spin degeneracy and $n_{a\sigma}$ is the number of elections in the adsorbate energy level. As usually we assume S_{ad} $= -\alpha * V_{ad}$ and take $V_{ad}^2 = \beta * V_{ratio}$, where V_{ratio} is the relative coupling strengths to pure Cu $\frac{V_{ad}^2}{V_{aCu}^2}$ for a given adsorbate. The introduction of β will decrease the number of unknown parameters and thus simplifying the model.

4.2.2 Bayesian Inference

There are a number of unknown parameters in the Newns-Anderson model discussed above, including the interatomic coupling and overlap matrix elements (V_{ak}, S_{ak}), the image potential (V_{im}), the effective intra-atomic Coulomb repulsion (U_{eff}), along with linear function coefficients within $f(\langle n_{a,\sigma}\rangle, \langle n_{a,-\sigma}\rangle)$ for correcting the electron correlation energy. All those parameters can be estimated from databases, tables, or simple calculations, as prior knowledge. For example, V_{ak} can be computed from DFT with localized basis sets, but it is intractable due to the existence of a large number of states and thus beats the purpose of extracting insights. It can also be estimated using the Solid State table within the tight-binding approximation. By fitting the adsorbate density of states from the Newns-Anderson model (Eq. 4.3) to that from DFT calculations, the Santos-Schmickler model has been developed to understand H_2 evolution/oxidation [68, 109], and OH^- adsorption on metal surfaces [110]. However, the deterministic fitting is likely trapped by local minima, thus limited to simple models. We used the Bayesian approach to infer unknown parameters from evidence, i.e., ab initio electronic (e.g., projected density of states) and adsorption (e.g., ensemble adsorption energies) properties. Basically, all we do is to deduce the “causes” (parameters) from the “effects” (observations) based on physical models. In addition, the Bayesian approach [111] provides a natural framework for generating probabilistic estimates of latent variables while accounting for uncertainties and incorporating prior knowledge if available.

4.3 Results and discussion

Because of the scaling relations between adsorption energies of key reaction species, the binding energies of a single intermediate or two are often sufficient to describe the trend of catalytic activity/selectivity, greatly simplifying the process of searching for new catalysts[112].

For example, adsorption energy of molecule AH_x is linearly correlated with the adsorption energy of atom A on a range of close-packed and stepped metal surfaces, where A can be C, N , O, S[20]. While the correlations between adsorbed species bring benefits to the description of catalysts properties, they could also cause trouble to the catalytic process, like the sluggish kinetics of a reaction originates from the linear energy scalings of key species. These theoretical scaling relations suggest the catalytic performance would exhibit volcano-shaped relationships with respect to the reactivity descriptor and tune one specific specie will according affect other species. Thus it is always challenging to improve the catalysts performance by breaking the scaling relationship. In this project, we try to answer two questions: (1) Why some adsorbed intermediates are linearly scaled with each other; (2) How to break this correlation. Here we will take *O and *OH species as example.

*O and *OH adsorption on {111}-terminated metal surfaces hold good correlation as seen in Fig. 4.2. After we developed a model to find governing electronic structure for adsorption energy of each intermediate, we'll have highly chance to break this scaling relationship.

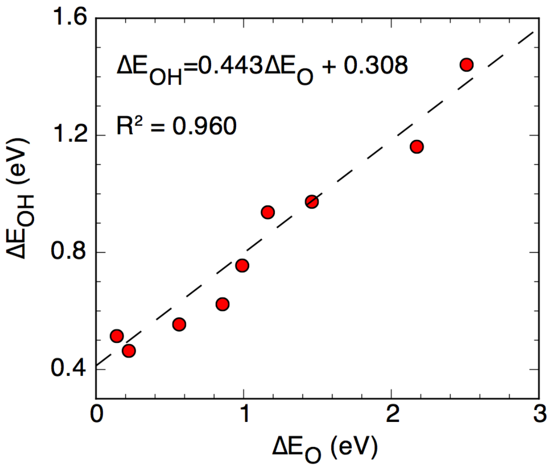

Figure 4.2: The binding energies of *O vs. *OH on {111}-terminated metal surfaces relative to H_2, H_2O.

Bayesian learning begins with a pre-existing probability distribution, called the prior. A finite amount of data can then be taken into consideration, leading to the posterior distribution. Computing the absolute probability of a sampling is difficult in most scenarios. To avoid this complication, the Markov Chain Monte Carlo (MCMC) method [113], whose acceptance criterion only depends on the relative probability, is typically used to sample from the posterior distribution of latent variables. Due to the computationally intensive nature of the MCMC algorithm, there is a need for a more efficient implementation of the Newns-Anderson model than what is obtained by Python and standard libraries like SciPy and NumPy. We make extensive use of Cython, a `C++` extension to the standard Python, to speed up the performance (10−1000 times) of some CPU-intensive functions in the model, e.g., Hilbert transform. To perform MCMC sampling, we use PyMC, a flexible and extensible Python package which includes a wide selection of built-in statistical distributions and sampling algorithms [114], e.g., Metropolis. A "burn-in" of 250 K samplings was discarded to ensure that subsequent ones are representative of the posterior distribution. Convergence of our MCMC-based sampling and stopping rule was verified using a consistent batch means approach [115]. The MCMC sampling results can be directly visualized using *corner*, a open-source Python module. In Fig. 4.3, we are showing the posterior parameter distribution of a slightly simplified model using only ΔE_{sp}, ϵ_a, α and β for *O adsorption on {111}-terminated transition metals. We ignored the spin for simplicity. We define the cost function directly using the projected O^{2p}

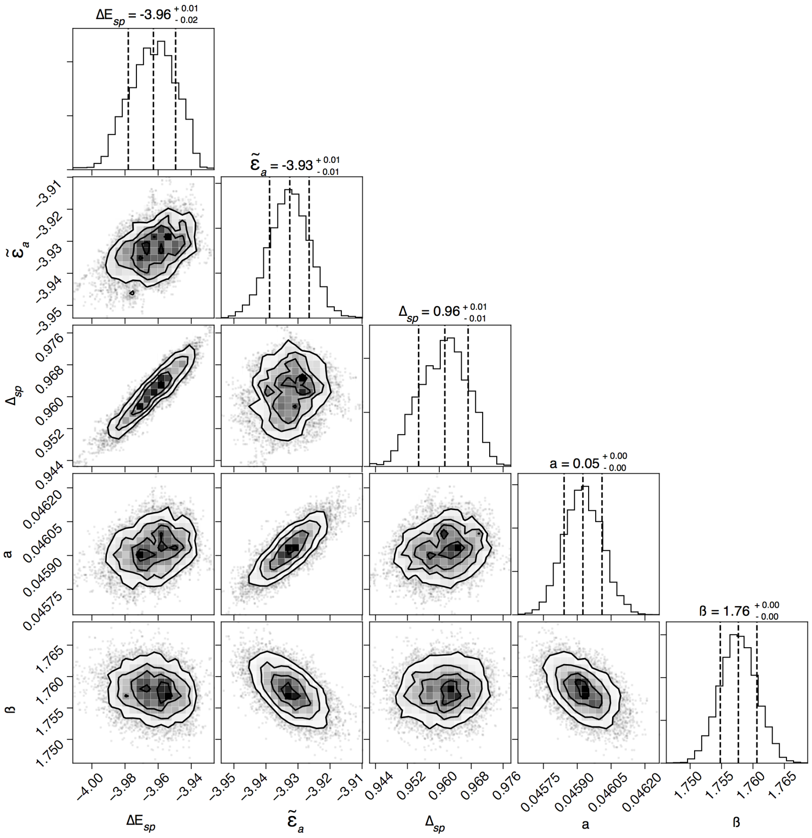

Figure 4.3: (a) The co-variances and 1D histograms of joint posterior distributions of the model parameters (ΔE_{sp}, $\tilde{\epsilon}_a$, Δ_{sp}, α, and β) from MCMC simulations for *O adsorption at the fcc-hollow site of transition metals.

density of states and binding energy of O on a series of transition metals as "observations". After convergence (∼500 K iterations), the histograms of MCMC samples for model parameters are shown in the diagonal, while the approximate contours for 68%, 95%, and 99% confidence regions are shown at lower triangle.

4.3.1 *O adsorbed on the transition metals

In this case, we need to consider the degeneracy of O^{2p} orbital which is three, the explicit equation to calculate binding energy of *O becomes:

$$\begin{aligned}\Delta E_O &= \Delta E_{sp} + \Delta E_d \\ &= \Delta E_s p + ((\frac{2}{\pi}\int_{-\infty}^{0} \text{Arc}\tan(\frac{\Delta(\epsilon)}{\epsilon - \epsilon_{a\sigma} - \Lambda(\epsilon)})\, \mathrm{d}\epsilon - n_{a\sigma}\epsilon_{a\sigma}) + (2 * (1+f) * \alpha * V_{ad}^2)) * 3\end{aligned} \tag{4.7}$$

In Fig. 4.4(a), it shows the model predicted projected density of states of O^{2p} on a series of {111}-terminated transition metals (Au, Ag, Cu, Pt, Pd, Ni, Ir,Rh,Co), which resembles with that from DFT calculations with clearly captured bonding and anti-bonding signatures. In Fig. 4.4(b), it shows the model

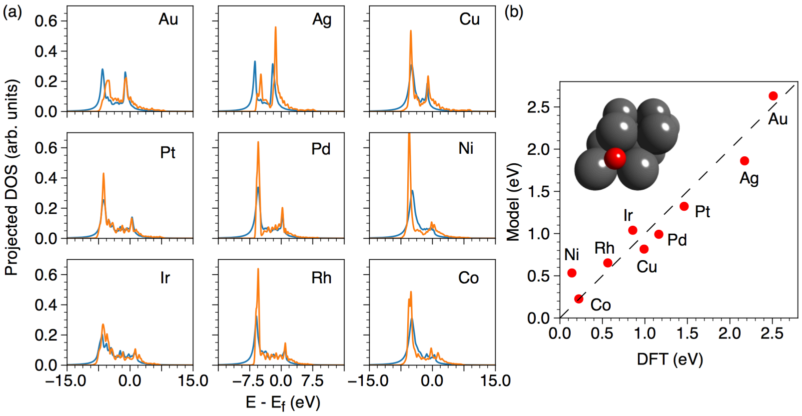

Figure 4.4: (a) Projected O^{2p} density of states from Bayesian learning(blue) and DFT calculations(orange). (b) DFT-calculated vs. model-predicted *O free formation energies on {111}-terminated transition metals

predicted adsorption energies of O on the hollow site of those metals, which agrees well with the DFT calculated binding energies. In this system, there are four unknown parameters: *sp*-band contribution ΔE_{sp}, energy level of O ϵ_a, overlap constant α and coupling strength ratio β. All four parameters are assumed to be independent of metal surfaces and taken as the constant in the training system.

4.3.2 *OH adsorbed on the transition metals

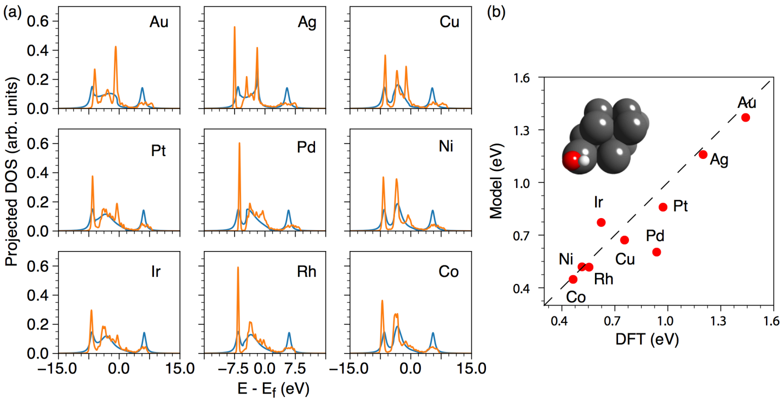

Figure 4.5: (a) Projected molecular orbital OH density of states from Bayesian learning(blue) and DFT calculations(orange). (b) DFT-calculated vs. model-predicted *OH free formation energies on {111}-terminated transition metals

In the system of OH adsorption on the transition metals, instead of using atomic orbital, we shift to molecular orbitals. It suggests orbital 3σ, 4π and $5\sigma^*$ are mainly responsible for the bonding to the metal surfaces[67]. Therefore, we'll have three different ϵ_a and β corresponding to these three orbitals. The parameter α characterizing orthogonalization of two orbitals can be assumed to be universal for different molecular orbitals[108]. ΔE_{sp} is the overall interaction between three molecular orbitals with *sp*-band of metals, as shown in Eq. 4.8. And the target projected density of states is the summation of O^{2p} and H^{2s} on a series of {111}-terminated transition metals (Au, Ag, Cu, Pt, Pd, Ni, Ir,Rh,Co). In Fig. 4.5(a), it shows the model predicted projected density of states of OH , which resembles with that from DFT calculations with clearly captured bonding and anti-bonding signatures.

In Fig. 4.5(b), it shows the model predicted adsorption energies of OH on the top site of those metals.

$$\begin{aligned}\Delta E_{OH} &= \Delta E_{sp} + \Delta E_{d} \\ &= \Delta E_{sp} + \Delta E_{d3\sigma} + \Delta E_{d4\pi} + \Delta E_{d5\sigma*} \end{aligned} \tag{4.8}$$

$$\Delta E_{d3\sigma} = (\frac{2}{\pi}\int_{-\infty}^{0} \text{Arc tan}(\frac{\Delta(\epsilon)}{\epsilon - \epsilon_{3\sigma} - \Lambda(\epsilon)})\, \mathrm{d}\epsilon - n_{3\sigma}\epsilon_{3\sigma}) + (2*(1+f)*\alpha*V_{3\sigma d}^2) \tag{4.9}$$

$$\Delta E_{d4\pi} = ((\frac{2}{\pi}\int_{-\infty}^{0} \text{Arc tan}(\frac{\Delta(\epsilon)}{\epsilon - \epsilon_{4\pi} - \Lambda(\epsilon)})\, \mathrm{d}\epsilon - n_{4\pi}\epsilon_{4\pi}) + (2*(1+f)*\alpha*V_{4\pi d}^2))*2 \tag{4.10}$$

$$\Delta E_{d5\sigma*} = (\frac{2}{\pi}\int_{-\infty}^{0} \text{Arc tan}(\frac{\Delta(\epsilon)}{\epsilon - \epsilon_{5\sigma*} - \Lambda(\epsilon)})\, \mathrm{d}\epsilon - n_{5\sigma*}\epsilon_{5\sigma*}) + (2*(1+f)*\alpha*V_{5\sigma*d}^2) \tag{4.11}$$

4.3.3 Density of states reconstruction and Sobol sensitivity

One advantage of using the Bayesian model of chemisorption is its capability to unravel practically tunable factors of surface reactivity. Within the Bayesian framework, we infer orbitalwise interactions that are highly influential on free formation energies of key reaction species by employing the Sobol sensitivity analysis approach [118]. This analysis has been very useful for machine learning practitioners and data scientists to interpret complicated

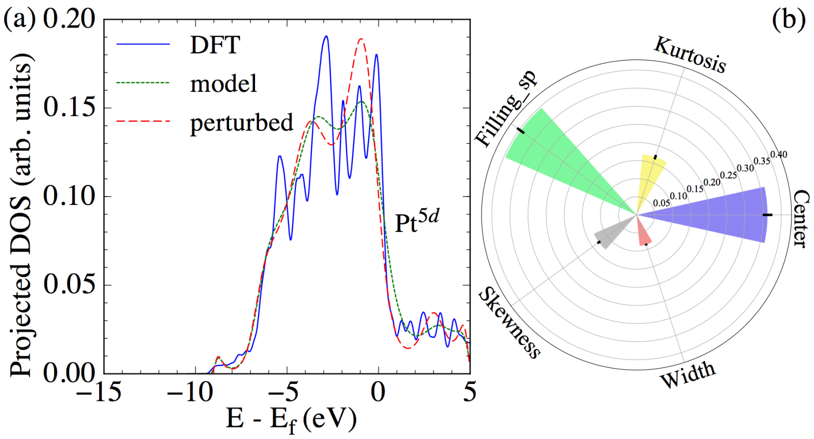

Figure 4.6: (a) The reconstruction of density of states from moments using the maximum entropy algorithm. The projected d-states distribution of Pt(100) from DFT is shown together with the model distribution reconstructed from 15 lowest moments with and without a +2% perturbation to the band center ϵ_d. (b) Sobol sensitivity analysis of the Gaussian process regression model for *N free formation energies on Pt model alloys.

models in many applications, such as biological systems [119], pharmacology [120], and risk assessments [121]. In essence, the Sobol sensitivity analysis is a probabilistic approach that quantifies the contribution of individual variables and their high-order couplings to the variance of the model output(s) using Monte Carlo sampling [118, 122].

The electron correlation effects can be included within the second-order perturbation approach of Brenig and Schonhammer [123] or a linear model to the orbital occupancy [68, 109]. In this project, we're currently working on generalizing model Hamiltonians to metal-electrolyte interfaces. Our preliminary results have shown the filling and center are two important electronic factors governing the chemical bond trend, Fig. 4.6

4.4 Conclusion

To conclude, we develop a Bayesian chemisorption model by learning from ab initio data. Compared with the purely data-driven model, the new model showed improved performance for describing the surface reactivity of multimetallics attributed to its explicit consideration of interatomic interactions and distribution of density of states. Moreover, the model sheds light on the nature of chemical bonding, and thus provides a general framework to interpret complex nature of chemical bonding at surfaces. This study opens up the possibility of developing adsorbate-specific descriptors and a new way for unraveling trends of the surface reactivity of metal nanocatalysts with defects, impurities, alloy additions, supports, etc. Including multiple-atom adsorbates [124, 125, 126] relevant to electrochemistry is currently under going.

Bibliography

[1] M. Haruta, T. Kobayashi, H. Sano, and N. Yamada, "Novel gold catalysts for the oxidation of carbon monoxide at a temperature far below 0 °c," *Chem. Lett.*, vol. 16, no. 2, pp. 405–408, Feb. 1987.

[2] M. Valden, X. Lai, and D. W. Goodman, "Onset of catalytic activity of gold clusters on titania with the appearance of nonmetallic properties," *Science*, vol. 281, no. 5383, pp. 1647–1650, Sep. 1998.

[3] M. Mavrikakis, P. Stoltze, and J. K. Nørskov, "Making gold less noble," *Catal. Letters*, vol. 64, no. 2-4, pp. 101–106, Feb. 2000.

[4] D. Ricci, A. Bongiorno, G. Pacchioni, and U. Landman, "Bonding trends and dimensionality crossover of gold nanoclusters on metal-supported MgO thin films," *Phys. Rev. Lett.*, vol. 97, no. 3, p. 036106, Jul. 2006.

[5] G. C. Bond, C. Louis, and D. T. Thompson, *Catalysis by Gold.* Singapore, SINGAPORE: Imperial College Press, 2006.

[6] D. G. Truhlar, B. C. Garrett, and S. J. Klippenstein, "Current status of Transition-State theory," *J. Phys. Chem.*, vol. 100, no. 31, pp. 12 771–12 800, Jan. 1996.

[7] X. Ma and H. Xin, "Orbitalwise coordination number for predicting adsorption properties of metal nanocatalysts," *Phys. Rev. Lett.*, vol. 118, no. 3, p. 036101, Jan. 2017.

[8] J. Enkovaara, C. Rostgaard, J. J. Mortensen, J. Chen, M. Dułak, L. Ferrighi, J. Gavnholt, C. Glinsvad, V. Haikola, H. A. Hansen, H. H. Kristoffersen, M. Kuisma, A. H. Larsen, L. Lehtovaara, M. Ljungberg, O. Lopez-Acevedo, P. G. Moses, J. Ojanen,

T. Olsen, V. Petzold, N. A. Romero, J. Stausholm-Møller, M. Strange, G. A. Tritsaris, M. Vanin, M. Walter, B. Hammer, H. Häkkinen, G. K. H. Madsen, R. M. Nieminen, J. K. Nørskov, M. Puska, T. T. Rantala, J. Schiøtz, K. S. Thygesen, and K. W. Jacobsen, "Electronic structure calculations with GPAW: a real-space implementation of the projector augmented-wave method," *J. Phys. Condens. Matter*, vol. 22, no. 25, p. 253202, Jun. 2010.

[9] J. J. Mortensen, L. B. Hansen, and K. W. Jacobsen, "Real-space grid implementation of the projector augmented wave method," *Phys. Rev. B Condens. Matter*, vol. 71, no. 3, p. 035109, Jan. 2005.

[10] H. J. Monkhorst and J. D. Pack, "Special points for brillouin-zone integrations," *Phys. Rev. B Condens. Matter*, vol. 13, no. 12, pp. 5188–5192, Jun. 1976.

[11] X. Ma and H. Xin, "Orbitalwise coordination number for predicting adsorption properties of metal nanocatalysts," *Phys. Rev. Lett.*, vol. 118, no. 3, p. 036101, Jan. 2017.

[12] T. Bligaard, J. Nørskov, S. Dahl, J. Matthiesen, C. Christensen, and J. Sehested, "The Brønsted-Evans-Polanyi relation and the volcano curve in heterogeneous catalysis," *J. Catal.*, vol. 224, no. 1, pp. 206–217, May 2004. [Online]. Available: http://www.sciencedirect.com/science/article/B6WHJ-4C4BK02-2/2/dccf62e0a9ba8f28beb5c2d8faeee3c3

[13] F. Calle-Vallejo and M. T. M. Koper, "Theoretical Considerations on the Electroreduction of CO to C_2 Species on Cu(100) Electrodes," *Angew. Chem. Int. Ed.*, vol. 52, no. 28, pp. 7282–7285, Jul. 2013. [Online]. Available: http://onlinelibrary.wiley.com/doi/10.1002/anie.201301470/abstract

[14] B. Hammer and J. K. Nørskov, "Electronic factors determining the reactivity of metal surfaces," *Surf. Sci.*, vol. 343, no. 3, pp. 211–220, 10 Dec. 1995.

[15] T. Jiang, D. J. Mowbray, S. Dobrin, H. Falsig, B. Hvolbæk, T. Bligaard, and J. K. Nørskov, “Trends in CO oxidation rates for metal nanoparticles and Close-Packed, stepped, and kinked surfaces,” *J. Phys. Chem. C*, vol. 113, no. 24, pp. 10 548–10 553, Jun. 2009.

[16] F. Calle-Vallejo, J. I. Martínez, J. M. García-Lastra, P. Sautet, and D. Loffreda, “Fast prediction of adsorption properties for platinum nanocatalysts with generalized coordination numbers,” *Angew. Chem. Int. Ed.*, vol. 53, no. 32, pp. 8316–8319, Aug. 2014.

[17] M. G. Taylor, N. Austin, C. E. Gounaris, and G. Mpourmpakis, “Catalyst design based on morphology- and Environment-Dependent adsorption on metal nanoparticles,” *ACS Catal.*, vol. 5, no. 11, pp. 6296–6301, Nov. 2015.

[18] G. Mpourmpakis, A. N. Andriotis, and D. G. Vlachos, “Identification of descriptors for the CO interaction with metal nanoparticles,” *Nano Lett.*, vol. 10, no. 3, pp. 1041–1045, Mar. 2010.

[19] A. J. Medford, C. Shi, M. J. Hoffmann, A. C. Lausche, S. R. Fitzgibbon, T. Bligaard, and J. K. Nørskov, “CatMAP: A software package for Descriptor-Based microkinetic mapping of catalytic trends,” *Catal. Lett.*, vol. 145, no. 3, pp. 794–807, Mar. 2015.

[20] F. Abild-Pedersen, J. Greeley, F. Studt, J. Rossmeisl, T. R. Munter, P. G. Moses, E. Skúlason, T. Bligaard, and J. K. Nørskov, “Scaling properties of adsorption energies for hydrogen-containing molecules on transition-metal surfaces,” *Phys. Rev. Lett.*, vol. 99, no. 1, p. 016105, 6 Jul. 2007.

[21] W. T. Wallace and R. L. Whetten, “Coadsorption of CO and O2 on selected gold clusters: Evidence for efficient Room-Temperature CO2 generation,” *J. Am. Chem. Soc.*, vol. 124, no. 25, pp. 7499–7505, Jun. 2002.

[22] N. Austin and G. Mpourmpakis, “Understanding the stability and electronic and adsorption properties of subnanometer group XI monometallic and bimetallic catalysts,” *J. Phys. Chem. C*, vol. 118, no. 32, pp. 18 521–18 528, Aug. 2014.

[23] A. C. Lausche, A. J. Medford, T. S. Khan, Y. Xu, T. Bligaard, F. Abild-Pedersen, J. K. Nørskov, and F. Studt, “On the effect of coverage-dependent adsorbate–adsorbate interactions for CO methanation on transition metal surfaces,” *J. Catal.*, vol. 307, no. Supplement C, pp. 275–282, Nov. 2013.

[24] M. S. Daw and M. I. Baskes, “Semiempirical, quantum mechanical calculation of hydrogen embrittlement in metals,” *Phys. Rev. Lett.*, vol. 50, no. 17, pp. 1285–1288, Apr. 1983.

[25] B. Shan, L. Wang, S. Yang, J. Hyun, N. Kapur, Y. Zhao, J. B. Nicholas, and K. Cho, “First-principles-based embedded atom method for PdAu nanoparticles,” *Phys. Rev. B Condens. Matter*, vol. 80, no. 3, p. 035404, Jul. 2009.

[26] A. H. Larsen, J. J. Mortensen, J. Blomqvist, I. E. Castelli, R. Christensen, M. Dułak, J. Friis, M. N. Groves, B. Hammer, C. Hargus, E. D. Hermes, P. C. Jennings, P. B. Jensen, J. Kermode, J. R. Kitchin, E. L. Kolsbjerg, J. Kubal, K. Kaasbjerg, S. Lysgaard, J. B. Maronsson, T. Maxson, T. Olsen, L. Pastewka, A. Peterson, C. Rostgaard, J. Schiøtz, O. Schütt, M. Strange, K. S. Thygesen, T. Vegge, L. Vilhelmsen, M. Walter, Z. Zeng, and K. W. Jacobsen, “The atomic simulation environment—a python library for working with atoms,” *J. Phys. Condens. Matter*, vol. 29, no. 27, p. 273002, Jun. 2017.

[27] S. Wang, N. Omidvar, E. Marx, and H. Xin, “Coordination numbers for unraveling intrinsic size effects in gold-catalyzed CO oxidation,” *Phys. Chem. Chem. Phys.*, vol. 20, no. 9, pp. 6055–6059, Feb. 2018.

[28] B. Hvolbæk, T. V. W. Janssens, B. S. Clausen, H. Falsig, C. H. Christensen, and J. K. Nørskov, “Catalytic activity of au nanoparticles,” *Nano Today*, vol. 2, no. 4, pp. 14–18, Aug. 2007.

[29] Y. Maeda, T. Akita, and M. Kohyama, “High activity of Gold/Tin-Dioxide catalysts for Low-Temperature CO oxidation: Application of a reducible metal oxide to a catalyst support,” *Catal. Lett.*, vol. 144, no. 12, pp. 2086–2090, Dec. 2014.

[30] L.-C. Wang, L. He, Y.-M. Liu, Y. Cao, H.-Y. He, K.-N. Fan, and J.-H. Zhuang, “Effect of pretreatment atmosphere on CO oxidation over α-Mn2O3 supported gold catalysts,” *J. Catal.*, vol. 264, no. 2, pp. 145–153, Jun. 2009.

[31] J. Huang, C. Xue, B. Wang, X. Guo, and S. Wang, “Gold-supported tin dioxide nanocatalysts for low temperature CO oxidation: preparation, characterization and DRIFTS study,” *Reac Kinet Mech Cat*, vol. 108, no. 2, pp. 403–416, Apr. 2013.

[32] T. Uchiyama, H. Yoshida, Y. Kuwauchi, S. Ichikawa, S. Shimada, M. Haruta, and S. Takeda, “Systematic morphology changes of gold nanoparticles supported on CeO2 during CO oxidation,” *Angew. Chem. Int. Ed Engl.*, vol. 50, no. 43, pp. 10 157–10 160, Oct. 2011.

[33] S. Cao, F. F. Tao, Y. Tang, Y. Li, and J. Yu, “Size- and shape-dependent catalytic performances of oxidation and reduction reactions on nanocatalysts,” *Chem. Soc. Rev.*, vol. 45, no. 17, pp. 4747–4765, Aug. 2016.

[34] F. Yang, D. Deng, X. Pan, Q. Fu, and X. Bao, “Understanding nano effects in catalysis,” *Natl Sci Rev*, vol. 2, no. 2, pp. 183–201, Jun. 2015.

[35] B. R. Cuenya, “Synthesis and catalytic properties of metal nanoparticles: Size, shape,

support, composition, and oxidation state effects," *Thin Solid Films*, vol. 518, no. 12, pp. 3127–3150, Apr. 2010.

[36] F. Calle-Vallejo, D. Loffreda, M. T. M. Koper, and P. Sautet, "Introducing structural sensitivity into adsorption–energy scaling relations by means of coordination numbers," *Nat. Chem.*, vol. 7, no. 5, pp. 403–410, May 2015.

[37] H. Xin, A. Holewinski, and S. Linic, "Predictive Structure–Reactivity models for rapid screening of Pt-Based multimetallic electrocatalysts for the oxygen reduction reaction," *ACS Catal.*, vol. 2, no. 1, pp. 12–16, Jan. 2012.

[38] J. K. Nørskov, T. Bligaard, A. Logadottir, J. R. Kitchin, J. G. Chen, S. Pandelov, and U. Stimming, "Trends in the exchange current for hydrogen evolution," *J. Electrochem. Soc.*, vol. 152, no. 3, pp. J23–J26, Mar. 2005.

[39] N. M. Marković and P. N. Ross, "Surface science studies of model fuel cell electrocatalysts," *Surf. Sci. Rep.*, vol. 45, no. 4, pp. 117–229, Apr. 2002.

[40] V. Viswanathan and F. Y.-F. Wang, "Theoretical analysis of the effect of particle size and support on the kinetics of oxygen reduction reaction on platinum nanoparticles," *Nanoscale*, vol. 4, no. 16, pp. 5110–5117, Aug. 2012.

[41] J. Greeley, J. Rossmeisl, A. Hellmann, and J. K. Nørskov, "Theoretical trends in particle size effects for the oxygen reduction reaction," *Zeitschrift für Physikalische Chemie*, vol. 221, no. 9-10, pp. 1209–1220, Oct. 2007.

[42] T. Bligaard, J. K. Nørskov, S. Dahl, J. Matthiesen, C. H. Christensen, and J. Sehested, "The Brønsted–Evans–Polanyi relation and the volcano curve in heterogeneous catalysis," *J. Catal.*, vol. 224, no. 1, pp. 206–217, May 2004.

[43] J. Greeley, I. E. L. Stephens, A. S. Bondarenko, T. P. Johansson, H. A. Hansen, T. F. Jaramillo, J. Rossmeisl, I. Chorkendorff, and J. K. Nørskov, "Alloys of platinum and early transition metals as oxygen reduction electrocatalysts," *Nat. Chem.*, vol. 1, no. 7, pp. 552–556, Oct. 2009.

[44] J. K. Nørskov, J. Rossmeisl, A. Logadottir, L. Lindqvist, J. R. Kitchin, T. Bligaard, and H. Jónsson, "Origin of the overpotential for oxygen reduction at a Fuel-Cell cathode," *J. Phys. Chem. B*, vol. 108, no. 46, pp. 17 886–17 892, 1 Nov. 2004.

[45] A. Holewinski, H. Xin, E. Nikolla, and S. Linic, "Identifying optimal active sites for heterogeneous catalysis by metal alloys based on molecular descriptors and electronic structure engineering," *Curr. Opin. Chem. Eng.*, vol. 2, no. 3, pp. 312–319, Aug. 2013.

[46] V. Viswanathan, H. A. Hansen, J. Rossmeisl, and J. K. Nørskov, "Universality in oxygen reduction electrocatalysis on metal surfaces," *ACS Catal.*, vol. 2, no. 8, pp. 1654–1660, Aug. 2012.

[47] B. Hammer and J. K. Nørskov, "Why gold is the noblest of all the metals," *Nature*, vol. 376, p. 238, Jul. 1995.

[48] J. R. Kitchin, J. K. Norskov, M. A. Barteau, and J. G. Chen, "Role of strain and ligand effects in the modification of the electronic and chemical properties of bimetallic surfaces," *Phys. Rev. Lett.*, vol. 93, no. 15, p. 156801, Oct. 2004.

[49] F. Calle-Vallejo, J. Tymoczko, V. Colic, Q. H. Vu, M. D. Pohl, K. Morgenstern, D. Loffreda, P. Sautet, W. Schuhmann, and A. S. Bandarenka, "Finding optimal surface sites on heterogeneous catalysts by counting nearest neighbors," *Science*, vol. 350, no. 6257, pp. 185–189, Oct. 2015.

[50] J. Hutter, M. Iannuzzi, F. Schiffmann, and J. VandeVondele, “cp2k: atomistic simulations of condensed matter systems,” *WIREs Comput Mol Sci*, vol. 4, no. 1, pp. 15–25, Jan. 2014.

[51] J. P. Perdew, K. Burke, and M. Ernzerhof, “Generalized gradient approximation made simple,” *Phys. Rev. Lett.*, vol. 77, no. 18, pp. 3865–3868, Oct. 1996.

[52] B. Hammer, L. B. Hansen, and J. K. Nørskov, “Improved adsorption energetics within density-functional theory using revised Perdew-Burke-Ernzerhof functionals,” *Phys. Rev. B Condens. Matter*, vol. 59, no. 11, pp. 7413–7421, Mar. 1999.

[53] S. Goedecker, M. Teter, and J. Hutter, “Separable dual-space gaussian pseudopotentials,” *Phys. Rev. B Condens. Matter*, vol. 54, no. 3, pp. 1703–1710, Jul. 1996.

[54] S. Curtarolo, G. L. W. Hart, M. B. Nardelli, N. Mingo, S. Sanvito, and O. Levy, “The high-throughput highway to computational materials design,” *Nat. Mater.*, vol. 12, no. 3, pp. 191–201, Mar. 2013.

[55] H. T. Chung, D. A. Cullen, D. Higgins, B. T. Sneed, E. F. Holby, K. L. More, and P. Zelenay, “Direct atomic-level insight into the active sites of a high-performance PGM-free ORR catalyst,” *Science*, vol. 357, no. 6350, pp. 479–484, Aug. 2017.

[56] W. G. Hardin, D. A. Slanac, X. Wang, S. Dai, K. P. Johnston, and K. J. Stevenson, “Highly active, nonprecious metal perovskite electrocatalysts for bifunctional Metal-Air battery electrodes,” *J. Phys. Chem. Lett.*, vol. 4, no. 8, pp. 1254–1259, Apr. 2013.

[57] D. Li, H. Lv, Y. Kang, N. M. Markovic, and V. R. Stamenkovic, “Progress in the development of oxygen reduction reaction catalysts for Low-Temperature fuel cells,” *Annu. Rev. Chem. Biomol. Eng.*, vol. 7, no. 1, pp. 509–532, Jun. 2016.

[58] Y. P. Zhu, C. Guo, Y. Zheng, and S.-Z. Qiao, “Surface and interface engineering of Noble-Metal-Free electrocatalysts for efficient energy conversion processes,” *Acc. Chem. Res.*, vol. 50, no. 4, pp. 915–923, Apr. 2017.

[59] R. R. Adžić and J. X. Wang, “Structures of surface adlayers and oxygen reduction kinetics,” *Solid State Ionics*, vol. 150, no. 1, pp. 105–114, Sep. 2002.

[60] T. J. Schmidt, V. Stamenkovic, P. N. Ross, Jr, and N. M. Markovic, “Temperature dependent surface electrochemistry on pt single crystals in alkaline electrolyte,” *Phys. Chem. Chem. Phys.*, vol. 5, no. 2, pp. 400–406, Jan. 2003.

[61] J. Hutter, M. Iannuzzi, F. Schiffmann, and J. VandeVondele, “cp2k: atomistic simulations of condensed matter systems,” *WIREs Comput Mol Sci*, vol. 4, no. 1, pp. 15–25, 1 Jan. 2014.

[62] I. C. Man, H.-Y. Su, F. Calle-Vallejo, H. A. Hansen, J. I. Martínez, N. G. Inoglu, J. Kitchin, T. F. Jaramillo, J. K. Nørskov, and J. Rossmeisl, “Universality in oxygen evolution electrocatalysis on oxide surfaces,” *ChemCatChem*, vol. 3, no. 7, pp. 1159–1165, Jul. 2011.

[63] J. Rossmeisl, A. Logadottir, and J. K. Nørskov, “Electrolysis of water on (oxidized) metal surfaces,” *Chem. Phys.*, vol. 319, no. 1, pp. 178–184, Dec. 2005.

[64] M. T. M. Koper, “Thermodynamic theory of multi-electron transfer reactions: Implications for electrocatalysis,” *J. Electroanal. Chem.*, vol. 660, no. 2, pp. 254–260, Sep. 2011.

[65] A. J. Medford, A. Vojvodic, J. S. Hummelshøj, J. Voss, F. Abild-Pedersen, F. Studt, T. Bligaard, A. Nilsson, and J. K. Nørskov, “From the sabatier principle to a predictive

theory of transition-metal heterogeneous catalysis," *J. Catal.*, vol. 328, pp. 36–42, Aug. 2015.

[66] A. N. Andriotis, G. Mpourmpakis, S. Broderick, K. Rajan, S. Datta, M. Sunkara, and M. Menon, "Informatics guided discovery of surface structure-chemistry relationships in catalytic nanoparticles," *J. Chem. Phys.*, vol. 140, no. 9, p. 094705, Mar. 2014.

[67] H. Xin and S. Linic, "Communications: Exceptions to the *d*-band model of chemisorption on metal surfaces: The dominant role of repulsion between adsorbate states and metal d-states," *J. Chem. Phys.*, vol. 132, no. 22, pp. 221 101–221 101–4, Jun. 2010.

[68] E. Santos, P. Quaino, and W. Schmickler, "Theory of electrocatalysis: hydrogen evolution and more," *Phys. Chem. Chem. Phys.*, vol. 14, no. 32, pp. 11 224–11 233, 2012.

[69] M. Shao, A. Peles, and K. Shoemaker, "Electrocatalysis on platinum nanoparticles: particle size effect on oxygen reduction reaction activity," *Nano Lett.*, vol. 11, no. 9, pp. 3714–3719, Sep. 2011.

[70] A. Holewinski and S. Linic, "Elementary mechanisms in electrocatalysis: Revisiting the ORR tafel slope," *J. Electrochem. Soc.*, vol. 159, no. 11, pp. H864–H870, Jan. 2012.

[71] V. R. Stamenkovic, B. S. Mun, M. Arenz, K. J. J. Mayrhofer, C. A. Lucas, G. Wang, P. N. Ross, and N. M. Markovic, "Trends in electrocatalysis on extended and nanoscale pt-bimetallic alloy surfaces," *Nat. Mater.*, vol. 6, no. 3, pp. 241–247, Mar. 2007.

[72] V. R. Stamenkovic, B. Fowler, B. S. Mun, G. Wang, P. N. Ross, C. A. Lucas, and N. M. Marković, "Improved oxygen reduction activity on Pt3Ni(111) via increased surface site availability," *Science*, vol. 315, no. 5811, pp. 493–497, Jan. 2007.

[73] T. V. Cleve, S. Moniri, G. Belok, K. L. More, and S. Linic, "Nanoscale engineering of

efficient oxygen reduction electrocatalysts by tailoring the local chemical environment of pt surface sites," *ACS Catal.*, vol. 7, no. 1, pp. 17–24, Jan. 2017.

[74] C. Wang, M. Chi, D. Li, D. Strmcnik, D. van der Vliet, G. Wang, V. Komanicky, K.-C. Chang, A. P. Paulikas, D. Tripkovic, J. Pearson, K. L. More, N. M. Markovic, and V. R. Stamenkovic, "Design and synthesis of bimetallic electrocatalyst with multilayered pt-skin surfaces," *J. Am. Chem. Soc.*, vol. 133, no. 36, pp. 14 396–14 403, Sep. 2011.

[75] C. Cui, L. Gan, M. Heggen, S. Rudi, and P. Strasser, "Compositional segregation in shaped pt alloy nanoparticles and their structural behaviour during electrocatalysis," *Nat. Mater.*, vol. 12, no. 8, pp. 765–771, Aug. 2013.

[76] L. Zhang, R. Iyyamperumal, D. F. Yancey, R. M. Crooks, and G. Henkelman, "Design of pt-shell nanoparticles with alloy cores for the oxygen reduction reaction," *ACS Nano*, vol. 7, no. 10, pp. 9168–9172, Oct. 2013.

[77] L. Zhang and G. Henkelman, "Tuning the oxygen reduction activity of pd shell nanoparticles with random alloy cores," *J. Phys. Chem. C*, vol. 116, no. 39, pp. 20 860–20 865, Oct. 2012.

[78] J. K. Norsko, "Chemisorption on metal surfaces," *Rep. Prog. Phys.*, vol. 53, no. 10, p. 1253, Jan. 1999.

[79] B. Hammer and J. K. Nørskov, "Why gold is the noblest of all the metals," *Nature*, vol. 376, no. 6537, pp. 238–240, Jul. 1995.

[80] B. Hammer, Y. Morikawa, and J. K. Nørskov, "CO chemisorption at metal surfaces and overlayers," *Phys. Rev. Lett.*, vol. 76, no. 12, p. 2141, Mar. 1996.

[81] D. M. Newns, "Chemisorption on metals and its implications," *Phys. Bl.*, vol. 32, no. 12, pp. 611–619, Dec. 1976.

[82] S. G. Davison and K. W. Sulston, “Anderson-Newns-Grimley model,” in *Green-Function Theory of Chemisorption*, S. G. Davison and K. W. Sulston, Eds. Dordrecht: Springer Netherlands, 2006, pp. 45–74.

[83] M. Baldo, R. Pucci, F. Flores, G. Piccitto, and A. Martin-Rodero, “Simple solution to the Newns-Anderson hamiltonian of chemisorption,” *Phys. Rev. B Condens. Matter*, vol. 28, no. 12, pp. 6640–6646, Dec. 1983.

[84] J. P. Muscat and D. M. Newns, “Chemisorption on metals,” *Prog. Surf. Sci.*, vol. 9, no. 1, pp. 1–43, 1978.

[85] D. M. Newns, “Self-Consistent model of hydrogen chemisorption,” *Phys. Rev.*, vol. 178, no. 3, p. 1123, Feb. 1969.

[86] D. M. Edwards and D. M. Newns, “Electron interaction in the band theory of chemisorption,” *Phys. Lett. A*, vol. 24, no. 4, pp. 236–237, Feb. 1967.

[87] R. A. v. Santen and M. Neurock, “Theory of surface chemical reactivity,” *Russ. J. Phys. Chem. B*, vol. 1, no. 4, pp. 261–291.

[88] H. Xin, A. Vojvodic, J. Voss, J. K. Nørskov, and F. Abild-Pedersen, “Effects of *d*-band shape on the surface reactivity of transition-metal alloys,” *Phys. Rev. B Condens. Matter*, vol. 89, no. 11, p. 115114, Mar. 2014.

[89] J. R. Kitchin, J. K. Norskov, M. A. Barteau, and J. G. Chen, “Modification of the surface electronic and chemical properties of pt(111) by subsurface 3d transition metals,” *J. Chem. Phys.*, vol. 120, no. 21, pp. 10 240–10 246, Jun. 2004.

[90] M. Mavrikakis, B. Hammer, and J. K. Nørskov, “Effect of strain on the reactivity of metal surfaces,” *Phys. Rev. Lett.*, vol. 81, no. 13, pp. 2819–2822, Sep. 1998.

[91] J. Greeley, J. K. Norskov, and M. Mavrikakis, "ELECTRONIC STRUCTURE AND CATALYSIS ON METAL SURFACES," *Annu. Rev. Phys. Chem.*, vol. 53, no. 1, pp. 319–348, 2002.

[92] H. Xin, A. Holewinski, N. Schweitzer, E. Nikolla, and S. Linic, "Electronic structure engineering in heterogeneous catalysis: Identifying novel alloy catalysts based on rapid screening for materials with desired electronic properties," *Top. Catal.*, vol. 55, no. 5-6, pp. 376–390, Jun. 2012.

[93] P. W. Anderson, "Localized magnetic states in metals," *Phys. Rev.*, vol. 124, no. 1, p. 41, 1 Oct. 1961.

[94] M. C. Kennedy and A. O'Hagan, "Bayesian calibration of computer models," *J. R. Stat. Soc. Series B Stat. Methodol.*, vol. 63, no. 3, pp. 425–464, Aug. 2001.

[95] J. R. Kitchin, "Machine learning in catalysis," *Nature Catalysis*, vol. 1, no. 4, pp. 230–232, Apr. 2018.

[96] B. R. Goldsmith, J. Esterhuizen, J.-X. Liu, C. J. Bartel, and C. Sutton, "Machine learning for heterogeneous catalyst design and discovery," *AIChE J.*, vol. 64, no. 7, pp. 2311–2323, Jul. 2018.

[97] A. J. Medford, M. R. Kunz, S. M. Ewing, T. Borders, and R. R. Fushimi, "Extracting knowledge from data through catalysis informatics," *ACS Catal.*, Jun. 2018.

[98] D. S. Mebane, K. Sham Bhat, J. D. Kress, D. J. Fauth, M. L. Gray, A. Lee, and D. C. Miller, "Bayesian calibration of thermodynamic models for the uptake of CO2 in supported amine sorbents using ab initio priors," *Phys. Chem. Chem. Phys.*, vol. 15, no. 12, pp. 4355–4366, Jan. 2013.

[99] J. Wellendorff, K. T. Lundgaard, A. Møgelhøj, V. Petzold, D. D. Landis, J. K. Nørskov, T. Bligaard, and K. W. Jacobsen, "Density functionals for surface science: Exchange-correlation model development with bayesian error estimation," *Phys. Rev. B Condens. Matter*, vol. 85, no. 23, p. 235149, Jun. 2012.

[100] E. A. Walker, D. Mitchell, G. A. Terejanu, and A. Heyden, "Identifying active sites of the Water–Gas shift reaction over titania supported platinum catalysts under uncertainty," *ACS Catal.*, vol. 8, no. 5, pp. 3990–3998, May 2018.

[101] P. M. Lee, *Bayesian Statistics: An Introduction*, 4th ed. Wiley, Sep. 2012.

[102] R. Gomer, "Approaches to the theory of chemisorption," *Acc. Chem. Res.*, vol. 8, no. 12, pp. 420–427, Dec. 1975.

[103] T. B. Grimley, "Overlap effects in the theory of adsorption using anderson's hamiltonian," *J. Phys. C: Solid State Phys.*, vol. 3, no. 9, p. 1934, Mar. 2001.

[104] A. H. Larsen, J. Kleis, K. S. Thygesen, J. K. Nørskov, and K. W. Jacobsen, "Electronic shell structure and chemisorption on gold nanoparticles," *Phys. Rev. B Condens. Matter*, vol. 84, no. 24, p. 245429, Dec. 2011.

[105] P. Quaino and E. Santos, "Hydrogen evolution reaction on palladium multilayers deposited on au(111): A theoretical approach," *Langmuir*, vol. 31, no. 2, pp. 858–867, Jan. 2015.

[106] V. A. Margulis and E. E. Muryumin, "Chemisorption of single fluorine atoms on the surface of zigzag single-walled carbon nanotubes: A model calculation," *Physica B Condens. Matter*, vol. 390, no. 1, pp. 134–142, Mar. 2007.

[107] A. Vojvodic, J. K. Nørskov, and F. Abild-Pedersen, "Electronic structure effects in transition metal surface chemistry," *Top. Catal.*, vol. 57, no. 1, pp. 25–32, Feb. 2014.

[108] B. Hammer and J. K. Nørskov, “Theory of adsorption and surface reactions,” in *Chemisorption and Reactivity on Supported Clusters and Thin Films: Towards an Understanding of Microscopic Processes in Catalysis*, R. M. Lambert and G. Pacchioni, Eds. Dordrecht: Springer Netherlands, 1997, pp. 285–351.

[109] E. Santos and W. Schmickler, “Electrocatalysis of hydrogen Oxidation—Theoretical foundations,” *Angew. Chem. Int. Ed.*, vol. 46, no. 43, pp. 8262–8265, 5 Nov. 2007.

[110] L. M. C. Pinto, P. Quaino, M. D. Arce, E. Santos, and W. Schmickler, “Electrochemical adsorption of OH on pt(111) in alkaline solutions: combining DFT and molecular dynamics,” *Chemphyschem*, vol. 15, no. 10, pp. 2003–2009, Jul. 2014.

[111] S. Theodoridis, “Bayesian learning,” in *Machine Learning*. Elsevier, 2015, pp. 585–638.

[112] J. Greeley, “Theoretical heterogeneous catalysis: Scaling relationships and computational catalyst design,” *Annu. Rev. Chem. Biomol. Eng.*, vol. 7, pp. 605–635, Jun. 2016.

[113] W. R. Gilks, S. Richardson, and D. Spiegelhalter, *Markov Chain Monte Carlo in Practice*. CRC Press, 1 Dec. 1995.

[114] A. Patil, D. Huard, and C. J. Fonnesbeck, “PyMC: Bayesian stochastic modelling in python,” *J. Stat. Softw.*, vol. 35, no. 4, pp. 1–81, Jul. 2010.

[115] J. M. Flegal and G. L. Jones, “Batch means and spectral variance estimators in markov chain monte carlo,” *Ann. Stat.*, vol. 38, no. 2, pp. 1034–1070, Apr. 2010.

[116] X. Ma, Z. Li, L. E. K. Achenie, and H. Xin, “Machine-Learning-Augmented chemisorption model for CO2 electroreduction catalyst screening,” *J. Phys. Chem. Lett.*, vol. 6, no. 18, pp. 3528–3533, Sep. 2015.

[117] Z. Li, X. Ma, and H. Xin, "Feature engineering of machine-learning chemisorption models for catalyst design," *Catal. Today*, vol. 280, no. Part 2, pp. 232–238, Feb. 2017.

[118] I. M. Sobol , "Global sensitivity indices for nonlinear mathematical models and their monte carlo estimates," *Math. Comput. Simul.*, vol. 55, no. 1, pp. 271–280, Feb. 2001.

[119] A. Kiparissides, S. S. Kucherenko, A. Mantalaris, and E. N. Pistikopoulos, "Global sensitivity analysis challenges in biological systems modeling," *Ind. Eng. Chem. Res.*, vol. 48, no. 15, pp. 7168–7180, Aug. 2009.

[120] X.-Y. Zhang, M. N. Trame, L. J. Lesko, and S. Schmidt, "Sobol sensitivity analysis: A tool to guide the development and evaluation of systems pharmacology models," *CPT Pharmacometrics Syst Pharmacol*, vol. 4, no. 2, pp. 69–79, Feb. 2015.

[121] A. Tsanakas and P. Millossovich, "Sensitivity analysis using risk measures," *Risk Anal.*, vol. 36, no. 1, pp. 30–48, Jan. 2016.

[122] J. Herman and W. Usher, "SALib: An open-source python library for sensitivity analysis," *JOSS*, vol. 2, no. 9, p. 97, Jan. 2017.

[123] W. Brenig and K. Schönhammer, "On the theory of chemisorption," *Zeitschrift für Physik*, vol. 267, no. 3, pp. 201–208, Jun. 1974.

[124] P. Quaino, E. Santos, H. Wolfschmidt, M. A. Montero, and U. Stimming, "Theory meets experiment: Electrocatalysis of hydrogen oxidation/evolution at Pd–Au nanostructures," *Catal. Today*, vol. 177, no. 1, pp. 55–63, Nov. 2011.

[125] E. Santos, S. Bartenschlager, and W. Schmickler, "Electron transfer to heteronuclear diatomic molecules," *J. Electroanal. Chem.*, vol. 660, no. 2, pp. 314–319, Sep. 2011.

[126] E. Santos, M. T. M. Koper, and W. Schmickler, “Bond-breaking electron transfer of diatomic reactants at metal electrodes,” *Chem. Phys.*, vol. 344, no. 1–2, pp. 195–201, Feb. 2008.